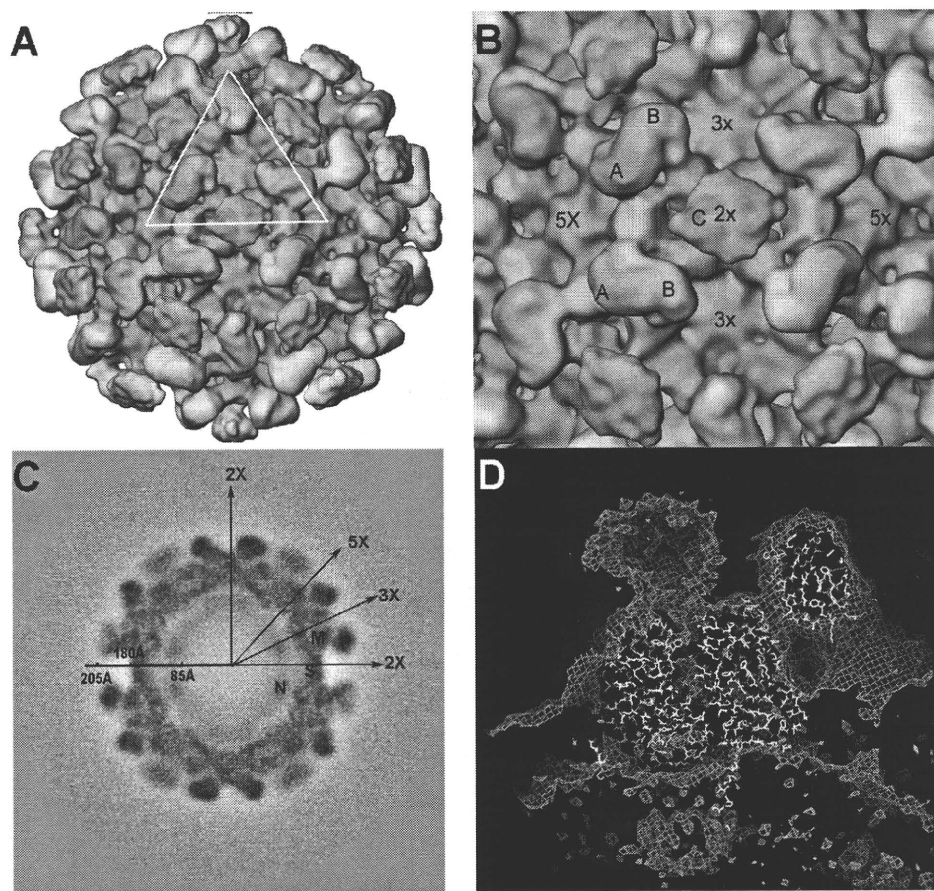FIGURE 2. **Three-dimensional structure of HEV T=3 VLP.** *A*, overall structure of the large HEV-VLP reveals the *T=3* icosahedral lattice of the ORF2 proteins. One icosahedral facet is defined as the *triangular area* within the three adjacent five-fold axes. *B*, there are two unique dimeric ORF2 spikes on the HEV T=3 VLP surface. The A-B dimer is located around the five-fold axis, and the C-C dimer is located at the two-fold axis. *C*, HEV T=3 VLP has a radius of 205 Å and contains a low density cavity with a radius of 85 Å in the particle center. The distribution of the cryo-EM density revealed four ORF2 domains, P, M, S, and N, at 50 Å from the equatorial section. *D*, the crystal structure of the HEV subunit from *T=1* VLP docks well with the cryo-EM density in the shell region of HEV *T=3* VLP, with the N-terminal loop pointing toward the center.

VLP is a *T=3* icosahedral particle (*T=3* VLP). We further performed element analysis with x-ray photo-electron spectroscopy. X-ray photo-electron spectroscopy, also known as electron spectroscopy for chemical analysis, determines the chemical composition of the sample with a depth of 50–70 nm. Phosphorus element, as a characteristic element of nucleic acid, was detected from the G3-VLP that was applied to the carbon-coated copper grid (supplemental Fig. 1C). Although the signal of phosphorus element is weak when compared with that of carbon, the phosphorus peak is not detectable in the control grid without VLP materials. This result suggests the co-existence of nucleic acid within the large G3-VLPs.

Three-dimensional Reconstruction of the HEV Virion-sized Particle— The cryo-EM structure of the large HEV-VLP revealed 90 protruding spikes on a complete icosahedral shell (Fig. 2A), which is consistent with the *T=3* icosahedral symmetry and the results of the STEM mass measurements. The VLP had an overall diameter of 410 Å and a central cavity of 170 Å in radius as measured from the three-dimensional density map (Fig. 2C). The single-layer capsid contained 180 copies of the ORF2 protein, which

cryo-electron micrographs, the images of HEV-VLP are decorated with spike-like features and are homogeneous in contrast (Fig. 1B).

To determine the composition of the large HEV-VLP, we performed mass measurements by using STEM, a technique that measures the amount of electrons scattered from the objects, such as VLPs, on an EM grid. A mixture of purified large and small HEV-VLPs was freeze-dried onto EM grids for STEM mass measurement. TMV with a known mass-to-length ratio was used as an internal standard. The HEV-VLPs appeared as spherical projections with white contrast on the dark field STEM images (Fig. 1A). White cloud-like objects were present in the background, which might be the VLPs broken during sample preservation. The mean mass of large VLP and TMV in the images was measured to generate a plot of the mean TMV mass per unit length *versus* mean VLP mass per particle (Fig. 1A). A first-order fit was calculated, and the mass of the large HEV-VLP was determined to be 11.8 MDa (Fig. 1D). The mass of the genotype-3 ORF2 protein, which was recovered from the large VLP, was measured as 65.5 KDa by mass spectrometry (Fig. 1C). Therefore, the large HEV-VLP contains 180 copies of ORF2 proteins, suggesting that the large HEV-

were grouped into three unique monomers according to their geometric environments. Although monomers A and B formed dimeric spikes (A-B dimers) around each of the five-fold axes, two two-fold related C monomers formed a spike (C-C dimer) at each of the icosahedral two-fold axes (Fig. 2B). The surface lattices of ORF2 proteins in HEV *T=3* VLP were similar to the capsid arrangement of caliciviruses. When compared with the A-B dimer, the morphology of the HEV C-C dimer was less well defined, perhaps due to flexibility in the angle of the protruding domain toward the icosahedral shell.

The density map of the *T=3* VLP displayed four discrete domains, designated from the outside inward as P, M, S, and N, on a section 52 Å from the equatorial plane (Fig. 2C). The density profile of the P, M, and S domains displayed less variation from that observed in *T=1* HEV-VLP, and the docking of the crystal structure of the *T=1* PORF2 protein to the density map of *T=3* HEV-VLP showed a very good agreement between the two structures (Fig. 2D). The docking positioned N-terminal tail of the PORF2 protein at the capsid inner surface aligned well with the density linker in *T=3* VLP (Fig. 2D). The linker density served as a tag to connect the N domain with the icosahedral capsid, indicating the
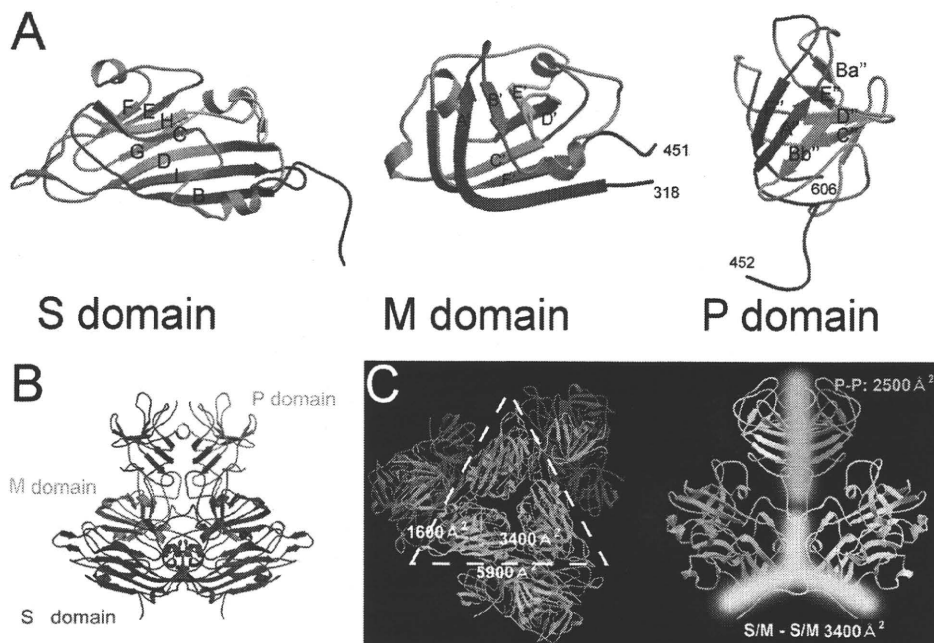
119

A

S domain   M domain   P domain

B

C

FIGURE 3. **The structure of genotype-1 PORF2 protein.** *A*, ribbon representations of S, M, and P. The structure is covered from *blue* (N terminus of the domain) to *red* (C terminus of the domain). *B*, dimer structure of the capsid protein. One subunit is colored *red*, and the other subunit is colored according to its domain structure (*blue*, S domain; *green*, M domain; *orange*, P domain). *C*, surface areas that buried at the interfaces between two adjacent subunits are overlapped with a PORF2 hexamer (*left*) and at the PORF2 dimeric interface (*right*). One icosahedral facet is defined as the *triangular area* within the three adjacent five-fold axes.

the S domain is the most conserved region among HEV genotypes, whereas greater divergence was seen in the N-terminal region (supplemental Fig. 4*A*). Among the solved structures, genotype-3 appeared flexible at the N-terminal end and was 11 amino acids shorter than the others, whereas the structure deviation from genotype-1 PORF2 is very small (total root mean square deviation is 0.62 for the 472 equivalent amino acids) (supplemental Fig. 4*B*). Because amino acids 118–129 play an important role in bridging the N-domain to the S-domain in $T=3$ VLP and serve as a docking register, we used the crystal structure of genotype-1 to decipher the $T=3$ cryo-EM density map.

Consistent Interdimeric Interactions between $T=3$ and $T=1$ HEV-VLPs—To understand the mechanism of ORF2 protein transition between $T=1$ and $T=3$ assem-

location of the N-terminal 111 amino acids of the ORF2 protein in $T=3$ HEV-VLP.

Crystal Structure of the Genotype-1 $T=1$ HEV-VLP—The crystal structure of the truncated genotype-1 capsid protein (PORF2, containing residues 112–608) can be separated into three domains, S, M, and P, with a less resolved region covering residues 555–560. The S domain formed by residues 118–317 folds into a classical eight-stranded β-barrel with a jelly roll motif (Fig. 3*A*), as observed in many $T=3$ viral capsid proteins (26, 27). Uniquely, three additional short α-helices were observed in the S domain between strands E and F and strands G and H. The capsid shell was mainly stabilized by intersubunit interactions between the S domains. The folded M domain, consisting of residues 318–451, was a twisted antiparallel β-sheet with an α-helix between the B′ and C′ strands (Fig. 3*A*). The P domain, composed of residues 452–606, folded into a β-barrel composed of antiparallel β-sheets, F″A″Bb″ and Ba″E″D″C″ (Fig. 3*A*), and was connected with the M domain through a long proline-rich hinge (PTPSPAPSRP of residues 452–461) (Fig. 3*A*). Although both the M and the P domains existed above the S domain, the protruding spikes in the HEV cryo-EM map contain only the P domain density, which is a clear difference to those caliciviruses (supplemental Fig. 3). The PORF2 dimers have the largest buried surface area between monomers (5,900 Å²) mainly due to the interface between P domains (Fig. 3*B*). The buried surface area is 3,400 and 1,600 Å² for the two adjacent PORF2 subunits around a three-fold axis and a five-fold axis, respectively (Fig. 3*B*). Moreover, the buried surface area of three molecules around a three-fold axis (9,500 Å²) is much wider than that around a five-fold axis (4,700 Å²).

Sequence alignment of genotype-1 PORF2 with the sequences of genotype-3 (10) and genotype-4 (11) revealed that

blies, we docked the $T=1$ decamer and hexamer into the $T=3$ cryo-EM density map. The decamer of $T=1$ VLP consisted of 10 adjacent PORF2 monomers corresponding to five dimers around a five-fold axis, whereas the $T=1$ hexamer corresponded to three adjacent dimers around a three-fold axis. Unlike the hexamer, the coordinates of the PORF2 decamer fitted very well with the curvature of the $T=3$ density map at the five-fold vertex (Fig. 4*A*) and with the domain separation (Fig. 4*B*). The curvature of $T=3$ capsid at the three-fold axis did not agree with the coordinates of the PORF2 hexamer as one of the dimers appeared to be sticking out of the cryo-EM density map (data not shown). Besides, the orientation of the P domain of the C-C dimer relative to its M/S domains was 90° different from that of the A-B dimer (Fig. 5). This suggests that the molecular interactions among A-B dimers in the $T=3$ icosahedron are consistent with the dimer-dimer interactions in the $T=1$ icosahedral assembly, whereas the interaction between the A-B dimer and C-C dimer is unique to the $T=3$ assembly.

In Vitro Reassembly of the ORF2 Protein—To understand the role of ORF2 decamer in $T=3$ VLP assembly, we analyzed the self-assembly process of HEV-VLP *in vitro*. A combination of chelating (EDTA) and reducing (DTT) agents was found to disassemble $T=3$ VLP in a high alkaline environment (pH 10) without denaturing the ORF2 protein (data not shown). The addition of 20 mM $CaCl_2$ into the disassembly solution led to the association of the ORF2 dimers into star-shaped complexes, and no refolded VLP was found (Fig. 4*C*). When we examined the star-shaped complexes, we found that the distance between two opposite vertices was ~18 nm, close to the diameter of TMV (Fig. 4*D*). This size was consistent with that measured from PORF2 decamers. Thus, the star-shaped complexes resembled not only the appearance but also the size of the ORF2
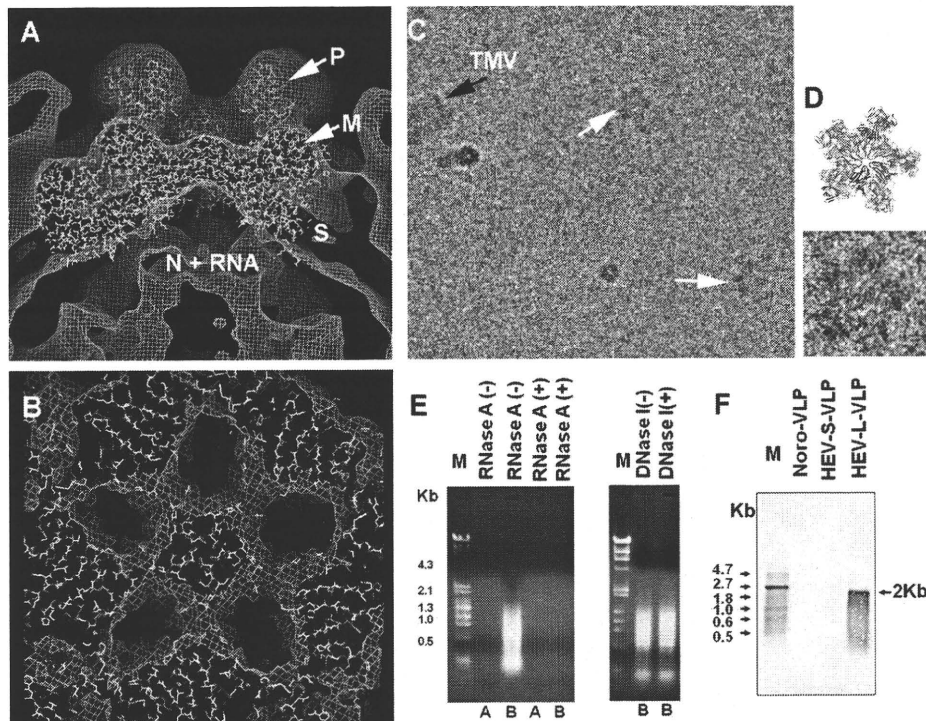
120

FIGURE 4. Structure of ORF2 decamer is consistent in both *T=1* and *T=3* VLPs. *A*, the cryo-EM density of HEV *T=3* VLP agrees well with the coordinates of *T=1* VLP at the region around the five-fold axis. The *P*, *M*, *S*, and *N + RNA* mark the corresponding density layer. *B*, consistent features between the decamer in HEV *T=3* and *T=1* VLP were revealed by the crystal structure docking of PORF2 dimers into the cryo-EM density map of HEV *T=3* VLP. *C*, reassembly of the ORF2 protein *in vitro* led to ORF2 star-shaped complex formation (*white arrows*). The size of this complex fits well into that of the ORF2 decamer after calibration with TMV (*black arrow*) as an internal standard. *D*, one ORF2 complex was zoomed in twice and is displayed in comparison with the crystal structure of PORF2 decamer (*ribbon drawing*). *E*, nucleic acids were extracted from HEV *T=1* VLP (*lane A*) and *T=3* VLP (*lane B*) and degraded in the presence of RNase A but remained as intact when incubated with DNase I. No nucleic acid was detected from *T=1* VLP (*lane A*). DNA maker (*lane M*): λ-HindIII + φ-174 HincII. *F*, Northern blotting to detect HEV RNA. RNA marker (*lane M*): 0.5–10-kb RNA ladder. RNA extract from large HEV *T=3* VLP, small HEV *T=1* VLP, and noravirus VLP was loaded in lane marked with *HEV-L-VLP*, *HEV-S-VLP*, and *nora-VLP*, respectively.

decamer (a pentamer of dimers). Although the overall buried surface area around the three-fold axis is larger than that around the five-fold axis, we did not find any complexes that could fit with the PORF2 hexamer.

The *in vitro* disassembly and reassembly suggested that other factors than ORF2 protein contribute to *T=3* VLP assembly. Considering the electropositivity of the ORF2 N-terminal 111 amino acids, we performed nucleic acid extraction from both the *T=3* and the *T=1* VLPs. Electrophoresis results demonstrated the presence of nucleic acids in the *T=3* extract, whereas the *T=1* VLP extract was negative for nucleic acids (Fig. 4*E*). The extracted nucleic acids were sensitive to RNase treatment and resistant to DNase treatment. To further characterize the nucleic acid, we performed Northern blotting according to the protocol described under "Experimental Procedures." An RNA band about 2 kb in size was detected from large particles, whereas no band was detected from the small particles and the control norovirus-like particles (Fig. 4*F*). This result is consistent with the VLP profiles observed from the cryo-electron micrographs and further indicated that the *T=3* particles encapsulated the HEV gene encoding the ORF2 protein.

DISCUSSION

Hepatitis E virus is a human pathogen that causes acute liver failure. Like other hepatitis viruses, HEV cannot be propagated with currently available cell culture techniques. The capsid protein of genotype-3 HEV can be expressed in insect cells as PORF2 protein, including amino acids 112–608 that self-assemble into *T=1* VLP, and as ORF2 protein, including amino acids 14–608 that form *T=3* VLP.

The crystal structures of PORF2 revealed three functional domains, S, M, and P, and the function of each domain constrained its sequence flexibility. The S domain formed an icosahedral shell that served as the base for arranging M and P domains; hence, the subunit surface should be highly conserved among genotypes. Sequence alignment agreed very well with this function, identifying the S domain as the most conserved region among HEV genotypes (28). The P domain serves as the putative binding site for both neutralizing antibody and cellular receptor (29) and contains 19 divergent amino acids across four genotypes (supplemental Fig. 4). Only nine of these amino acids were exposed at the surface of the P domain. Inspection of the binding footprint of antibodies on the cryo-EM density map indicated that only one amino acid was buried within the antibody-binding interface[4]. This explains why the HEV serotype is non-divergent despite sequence variation among HEV genotypes. The direct correlation between sequence variability and domain functionality may be necessary for the HEV capsid to carry multiple functions and to ensure error-free assembly. It also explains why the transition of HEV-VLP from the *T=3* to the *T=1* lattice does not disturb its antigenicity and why *T=1* VLP can be disassembled and reassembled *in vitro* to carry foreign antigenic epitopes (30) or DNA plasmids (31).

The *T=3* HEV-VLP has a similar morphology to that of calicivirus; however, the crystal structures of PORF2 revealed a distinctive M domain arrangement, although the folding of the HEV M domain is similar to the folding of the P1 domain in caliciviruses (supplemental Fig. 3). In HEV, the P domain is located at the C-terminal end of the M domain, whereas the P2 domain of caliciviruses is inserted into the P1 domain at the region between the A′ and B′ strands (32, 33). Furthermore, the M domain of HEV interacts strongly with the S domain and connects to the P domain via a long proline-rich hinge, whereas the P1 domain in caliciviruses is a subdomain of the protrusion
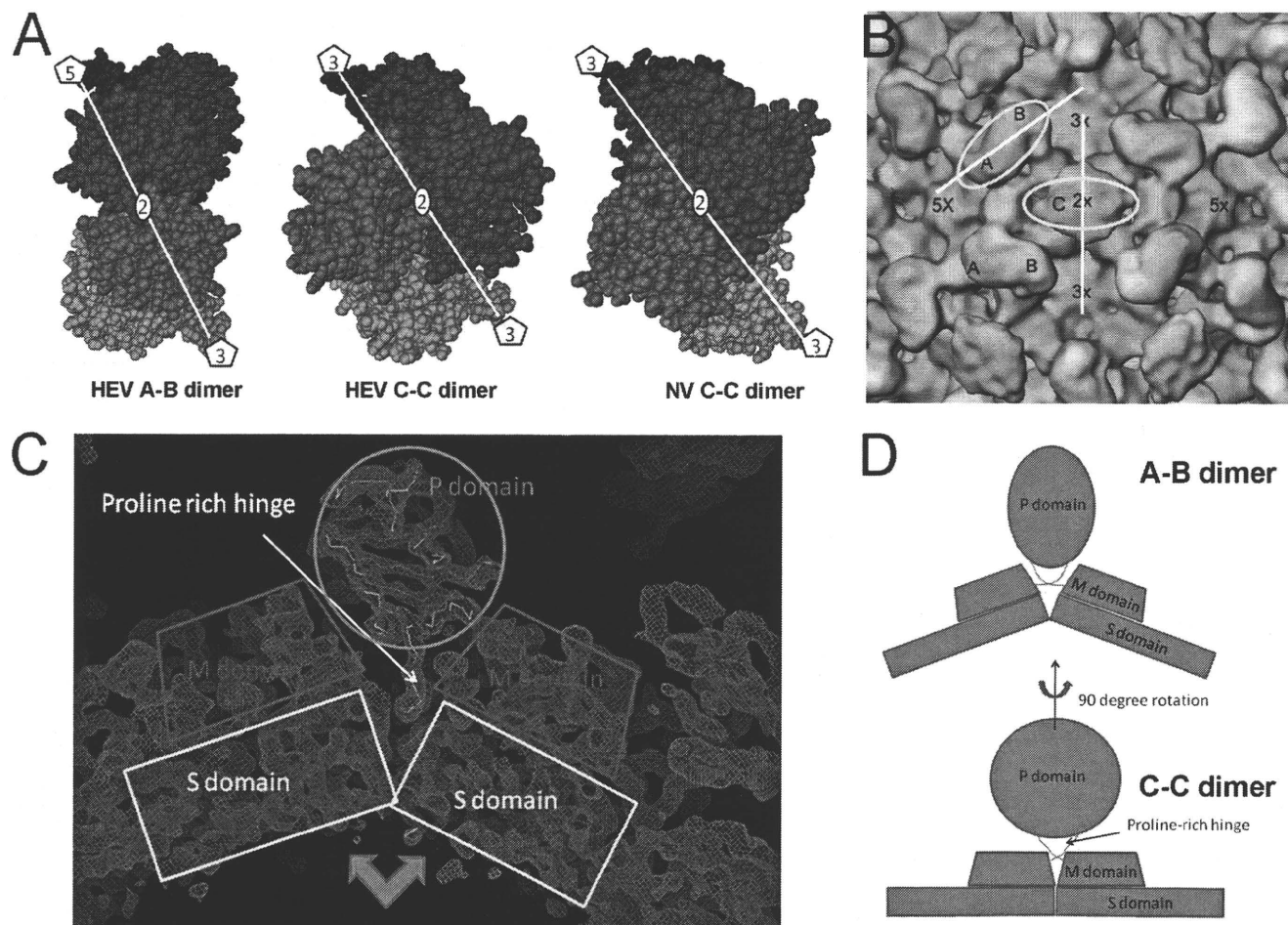
121

FIGURE 5. **The orientation of P domain relative to the M and S domain in the C-C dimer appears different from that in A-B dimer.** *A*, the dimeric interactions in the HEV A-B dimer, the HEV C/C dimers, and the Norwalk virus C-C dimer are shown in space-filling models as observed from the outside of the particles. S, M (P1) and P (P2) domains in a subunit are highlighted in *dark/light blue, dark/light green,* and *brown/chocolate,* respectively. *B*, in the *T=3* cryo-EM density map, the orientation of the P domain is shown as the angle between the platform of the spike (*yellow circles*) relative to the M/S domains in the C-C dimer (*white line* passing through the two adjacent three-fold axes) or the M/S domains in the A-B dimer (*white line* passing through a five-fold axis and the neighboring three-fold axis). *C*, the crystal density map showing the position of the proline-rich hinge within the cleft of the M domains. *D*, the cleft in between the M/S domains provides sufficient room to accommodate the proline-rich hinge in the A-B dimer, where the domains take a bent conformation. The cleft is narrowed down in the C-C dimer due to the flat conformation between the M/S domains, thus pushing the hinge up and out of the cleft.

spike (supplemental Fig. 3). This seems to have an impact on VLP stability; the spike of the HEV C-subunits appeared weakly defined when compared with that in the A-B dimer, whereas the spike of the Norwalk virus C-subunit appeared rigid and similar to that in the A-B dimer in the cryo-EM structure (34). Additionally, deletion of the N-terminal positively charged amino acids from the Norwalk virus capsid protein does not induce *T=1* VLP because the Norwalk virus capsid protein only contains a short N-terminal tail of 20 amino acids (35).The HEV C-C dimer is profoundly different from the HEV A-B dimer in the orientation of the P domain relative to the M/S domain (Fig. 5). Conformational difference between the A-B dimer and C-C dimer has been reported earlier *T=3* viruses. In tomato bushy stunt virus, binding of RNA plays an important role to differentiate the C-C dimer from the A-B dimer. The N-terminal arm of the C-C dimer is well ordered and interacts with the RNA genome, whereas the A-B dimer is disordered and free from RNA interactions (36). In the flock house virus, the C-C dimeric contact acquires a flat conformation to accom-

modate the RNA duplex, whereas the A-B dimer is in a bent conformation and involves no RNA (37). The different orientation observed between the HEV C-C dimer and A-B dimer may result from the difference in RNA occupancy. The A-B dimers do not interact with RNA and have a bent conformation. As a result, the angled contact of the M/S domains accommodated the proline-rich hinge within the V-shaped cleft, similar to that in the *T=1* VLP, thus solidifying the orientation of the P domain (Fig. 5C). In contrast, the contact with the RNA led the C-C dimer to a flat conformation that pushes the hinge out of the cleft. Thus, the P domain in the C-C dimer is flexible and could take a 90° rotation from the orientation in the A-B dimer (Fig. 5D).

The native HEV capsid was predicted to possess *T=3* icosahedral symmetry (8, 11), and Guu *et al.* (11) suggested that such *T=3* capsids require the dimer to have both flat and inwardly bent conformation at quasi-two-fold and icosahedral two-fold positions, respectively. Here, with detailed features, our cryo-EM structure of *T=3* VLP provided direct observation of
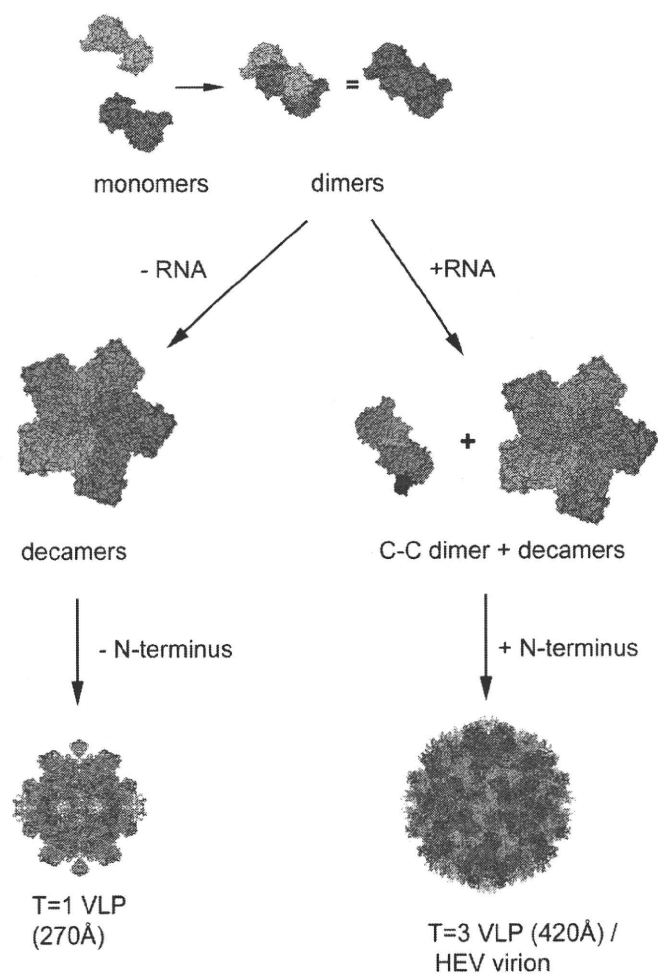
⧫ASBMB⧫

122

FIGURE 6. **Diagram showing the putative assembly process of HEV $T=1$ and $T=3$ VLP.** The ORF2 subunit encodes information that governs the assembly of decamers. Interaction with the RNA fragment induces flat dimeric contact and the formation of C-C dimers, which guides the assembly of the complete icosahedral capsid.

the two unique conformations between the A/B and C/C dimer at the foothold of S-domain contact but also in the arrangement of the protruding P-domain.

It is suggested by molecular simulation that $T=3$ icosahedral capsid assembly utilizes a mechanism in which preformed aggregates of intermediates combine in contrast to the formation of the $T=1$ icosahedral capsid that includes the addition of predominately monomers (38). The ORF2 decamer is therefore the assembly intermediate of $T=3$ HEV capsid and is located at each of the five-fold vertexes. The appearance of a hexameric ring at icosahedral three-fold positions is the critical step in $T=3$ capsid assembly and depends on the C-C dimer. The *in vitro* disassembly and reassembly also indicates the involvement of an extrinsic factor other than the ORF2 protein in the assembly of $T=3$ VLP and the C-C dimer is in a flat conformation that is concomitant with RNA binding. The induction of C-C conformation has been reported with bacteriophage MS2, where the complete assembly of capsid requires the presence of synthetic RNA fragment (39). Therefore, the pentamer of dimer (Fig. 4C) may be the assembly intermediate that is common for the $T=3$ virus. The interaction of RNA with the N-terminal end of ORF2 is the driving force leading the C-C dimer to

the flat formation and ultimately full capsid formation through the integration of 30 copies of C-C dimers with 12 copies of A-B decamers (Fig. 6).

The existence of the N-terminal amino acids 14–111 prevents ORF2 proteins from forming $T=1$ VLP. The capsid of $T=1$ VLP encloses a central cavity with a volume allowing a maximum of 55 additional residues on each copy of PORF2 protein, if the average protein density is considered to be 1.30 g/ml. The maximum diameter of the central cavity is about 340 Å for the $T=3$ VLP and thus is sufficient to accommodate both the HEV genome and the ORF2 N-terminal domains. By characterizing the size and the sequence of the encapsidated RNA, we found that the $T=3$ HEV VLP selectively encapsidated the RNA fragment that encodes the ORF2 protein. Thus, it is very possible that the native HEV capsid is the $T=3$ icosahedron. There, the encapsulated genomic RNA may play a direct role in the assembly of the HEV infectious virion. Our data demonstrated here that HEV was different from caliciviruses in its assembly pathway, protein domain arrangement, and genome organization, although both viruses are $T=3$ icosahedral particles with dimeric spikes. Hepatitis E virus showed a high similarity to some plant viruses in its assembly pathway: the utilization of a long electropositive N-terminal domain to interact with genomic RNA. Although the evolutionary origin for such similarities requires further investigation, our data place the HEV structure in a unique position, deviating from that of human caliciviruses and approaching that of $T=3$ small plant viruses.

REFERENCES

1. Naik, S. R., Aggarwal, R., Salunke, P. N., and Mehrotra, N. N. (1992) *Bull. World Health Organ* **70**, 597–604
2. Tam, A. W., Smith, M. M., Guerra, M. E., Huang, C. C., Bradley, D. W., Fry, K. E., and Reyes, G. R. (1991) *Virology* **185**, 120–131
3. Schofield, D. J., Purcell, R. H., Nguyen, H. T., and Emerson, S. U. (2003) *Vaccine* **22**, 257–267
4. Li, T. C., Suzaki, Y., Ami, Y., Dhole, T. N., Miyamura, T., and Takeda, N. (2004) *Vaccine* **22**, 370–377
5. Purdy, M. A., McCaustland, K. A., Krawczynski, K., Spelbring, J., Reyes, G. R., and Bradley, D. W. (1993) *J. Med. Virol.* **41**, 90–94
6. Riddell, M. A., Li, F., and Anderson, D. A. (2000) *J. Virol.* **74**, 8011–8017
7. Li, T. C., Yamakawa, Y., Suzuki, K., Tatsumi, M., Razak, M. A., Uchida, T., Takeda, N., and Miyamura, T. (1997) *J. Virol.* **71**, 7207–7213
8. Xing, L., Kato, K., Li, T., Takeda, N., Miyamura, T., Hammar, L., and Cheng, R. H. (1999) *Virology* **265**, 35–45
9. Li, T. C., Takeda, N., Miyamura, T., Matsuura, Y., Wang, J. C., Engvall, H., Hammar, L., Xing, L., and Cheng, R. H. (2005) *J. Virol.* **79**, 12999–13006
10. Yamashita, T., Mori, Y., Miyazaki, N., Cheng, R. H., Yoshimura, M., Unno, H., Shima, R., Moriishi, K., Tsukihara, T., Li, T. C., Takeda, N., Miyamura, T., and Matsuura, Y. (2009) *Proc. Natl. Acad. Sci. U.S.A.* **106**, 12986–12991
11. Guu, T. S., Liu, Z., Ye, Q., Mata, D. A., Li, K., Yin, C., Zhang, J., and Tao,

123

Y. J. (2009) *Proc. Natl. Acad. Sci. U.S.A.* **106,** 12992–12997

12. Balayan, M. S., Andjaparidze, A. G., Savinskaya, S. S., Ketiladze, E. S., Braginsky, D. M., Savinov, A. P., and Poleschuk, V. F. (1983) *Intervirology* **20,** 23–31

13. Li, T. C., Scotti, P. D., Miyamura, T., and Takeda, N. (2007) *J. Virol.* **81,** 10890–10896

14. Wall, J. S., Hainfeld, J. F., and Simon, M. N. (1998) *Methods Cell Biol.* **53,** 139–164

15. Wall, J. S., and Simon, M. N. (2001) *Methods Mol. Biol.* **148,** 589–601

16. Baker, T. S., and Cheng, R. H. (1996) *J. Struct. Biol.* **116,** 120–130

17. Ji, Y., Marinescu, D. C., Zhang, W., Zhang, X., Yan, X., and Baker, T. S. (2006) *J. Struct. Biol.* **154,** 1–19

18. Jones, T. A., Zou, J. Y., Cowan, S. W., and Kjeldgaard, M. (1991) *Acta Crystallogr. Sect. A* **47,** 110–119

19. Chacón, P., and Wriggers, W. (2002) *J. Mol. Biol.* **317,** 375–384

20. Wang, C. Y., Miyazaki, N., Yamashita, T., Higashiura, A., Nakagawa, A., Li, T. C., Takeda, N., Xing, L., Hjalmarsson, E., Friberg, C., Liou, D. M., Sung, Y. J., Tsukihara, T., Matsuura, Y., Miyamura, T., and Cheng, R. H. (2008) *Acta Crystallogr. Sect. F Struct. Biol. Cryst. Commun.* **64,** 318–322

21. Blow, D. M., Rossmann, M. G., and Jeffery, B. A. (1964) *J. Mol. Biol.* **8,** 65–78

22. Brünger, A. T., Adams, P. D., Clore, G. M., DeLano, W. L., Gros, P., Grosse-Kunstleve, R. W., Jiang, J. S., Kuszewski, J., Nilges, M., Pannu, N. S., Read, R. J., Rice, L. M., Simonson, T., and Warren, G. L. (1998) *Acta Crystallogr. D Biol. Crystallogr.* **54,** 905–921

23. Laskowski, R. A., Rullmannn, J. A., MacArthur, M. W., Kaptein, R., and Thornton, J. M. (1996) *J. Biomol. NMR.* **8,** 477–486

24. Kraulis, P. (1991) *J. Appl. Cryst.* **24,** 946–950

25. Merritt, E. A., and Murphy, M. E. (1994) *Acta Crystallogr. D Biol. Crystallogr.* **50,** 869–873

26. Rossmann, M. G., and Johnson, J. E. (1989) *Ann. Rev. Biochem.* **58,** 533–573

27. Harrison, S. C. (2001) *Curr. Opin. Struct. Biol.* **11,** 195–199

28. Zhai, L., Dai, X., and Meng, J. (2006) *Virus Res.* **120,** 57–69

29. He, S., Miao, J., Zheng, Z., Wu, T., Xie, M., Tang, M., Zhang, J., Ng, M. H., and Xia, N. S. (2008) *J. Gen. Virol.* **89,** 245–249

30. Niikura, M., Takamura, S., Kim, G., Kawai, S., Saijo, M., Morikawa, S., Kurane, I., Li, T. C., Takeda, N., and Yasutomi, Y. (2002) *Virology* **293,** 273–280

31. Takamura, S., Niikura, M., Li, T. C., Takeda, N., Kusagawa, S., Takebe, Y., Miyamura, T., and Yasutomi, Y. (2004) *Gene Ther.* **11,** 628–635

32. Chen, R., Neill, J. D., Estes, M. K., and Prasad, B. V. (2006) *Proc. Natl. Acad. Sci. U.S.A.* **103,** 8048–8053

33. Prasad, B. V., Hardy, M. E., Dokland, T., Bella, J., Rossmann, M. G., and Estes, M. K. (1999) *Science* **286,** 287–290

34. Prasad, B. V., Matson, D. O., and Smith, A. W. (1994) *J. Mol. Biol.* **240,** 256–264

35. Bertolotti-Ciarlet, A., White, L. J., Chen, R., Prasad, B. V., and Estes, M. K. (2002) *J. Virol.* **76,** 4044–4055

36. Timmins, P. A., Wild, D., and Witz, J. (1994) *Structure* **2,** 1191–1201

37. Fisher, A. J., and Johnson, J. E. (1993) *Nature* **361,** 176–179

38. Nguyen, H. D., Reddy, V. S., and Brooks, C. L., 3rd (2009) *J. Am. Chem. Soc.* **131,** 2606–2614

39. Stockley, P. G., Rolfsson, O., Thompson, G. S., Basnak, G., Francese, S., Stonehouse, N. J., Homans, S. W., and Ashcroft, A. E. (2007) *J. Mol. Biol.* **369,** 541–552

124

Spatial Configuration of Hepatitis E Virus Antigenic Domain[▽]

Li Xing,[1,2]† Joseph C. Wang,[1]† Tian-Cheng Li,[3] Yasuhiro Yasutomi,[4] James Lara,[5] Yury Khudyakov,[5] Darren Schofield,[6] Suzanne U. Emerson,[6] Robert H. Purcell,[6] Naokazu Takeda,[3] Tatsuo Miyamura,[3] and R. Holland Cheng[1]*

Molecular and Cellular Biology, University of California, Davis, California 95616[1]; Karolinska Institute Structural Virology, F68 University Hospital, SE-14186 Stockholm, Sweden[2]; Department of Virology II, National Institute of Infectious Disease, Tokyo 162, Japan[3]; Tsukuba Primate Research Center, National Institute of Biomedical Innovation, Ibaraki 305-0843, Japan[4]; Division of Viral Hepatitis, Centers for Disease Control and Prevention (CDC), Atlanta, Georgia 30333[5]; and Hepatitis Virus Section, National Institute of Allergy and Infectious Diseases, Bethesda, Maryland 208892[6]

Hepatitis E virus (HEV) is a human pathogen that causes acute hepatitis. When an HEV capsid protein containing a 52-amino-acid deletion at the C terminus and a 111-amino-acid deletion at the N terminus is expressed in insect cells, the recombinant HEV capsid protein can self-assemble into a T=1 virus-like particle (VLP) that retains the antigenicity of the native HEV virion. In this study, we used cryoelectron microscopy and image reconstruction to show that anti-HEV monoclonal antibodies bind to the protruding domain of the capsid protein at the lateral side of the spikes. Molecular docking of the HEV VLP crystal structure revealed that Fab224 covered three surface loops of the recombinant truncated second open reading frame (ORF2) protein (PORF2) at the top part of the spike. We also determined the structure of a chimeric HEV VLP and located the inserted B-cell tag, an epitope of 11 amino acids coupled to the C-terminal end of the recombinant ORF2 protein. The binding site of Fab224 appeared to be distinct from the location of the inserted B-cell tag, suggesting that the chimeric VLP could elicit immunity against both HEV and an inserted foreign epitope. Therefore, the T=1 HEV VLP is a novel delivery system for displaying foreign epitopes at the VLP surface in order to induce antibodies against both HEV and the inserted epitope.

Hepatitis E virus (HEV) is a causative agent of acute hepatitis in humans and is primarily transmitted via the fecal-oral route. HEV is thus resistant to the low pH and digestive enzymes associated with the stomach and gastrointestinal tract. HEV regularly causes epidemics in many tropical and subtropical countries. In India, 101 outbreaks were confirmed by serological analysis in the state of Maharashtra in the last 5 years (6), and the lifetime risk of HEV infection exceeds 60% (28). Sporadic cases have also been reported in regions where HEV is endemic, as well as in areas where it is not endemic. Although some of these cases were associated with travel, many cases involved patients without a history of travel to regions where HEV is endemic. Accumulating evidence suggests that sporadic infection occurs through a zoonotic route and is not limited to developing countries. Seroprevalence suggests hepatitis E infection may also be prevalent in high-income countries (21), such as the United States (17), the United Kingdom (3), and Japan (18). The overall mortality rate of HEV infection during an outbreak generally ranges from 1 to 15%, and the highest mortality occurs in pregnant women, with fatality rates of up to 30% (19).

The HEV virion is composed of a 7.2-kb single-stranded RNA molecule and a 32- to 34-nm icosahedral capsid. The HEV genome contains three open reading frames (ORFs).

The capsid protein, encoded by the second open reading frame (ORF2), located at the 3′ terminus of the genome, comprises 660 amino acids and is responsible for most capsid-related functions, such as assembly, host interaction, and immunogenicity. Recombinant ORF2 proteins can induce antibodies that block HEV infection in nonhuman primates (12, 27). Four major antigenic domains were predicted to be located within the C-terminal 268 amino acids of the ORF2 protein; one domain was experimentally identified as a neutralization epitope in the Sar-55 ORF2 capsid protein (25, 26). However, the minimal peptide needed to induce anti-HEV neutralizing antibodies contains residues 459 to 607 of the ORF2 protein (33), which is much longer than a linear antigenic epitope, suggesting that the neutralization epitope is conformational. Therefore, the detailed structure of the HEV capsid protein is required in order to understand the organization of HEV epitopes.

Currently, there are 1,600 HEV genomic sequences available through the International Nucleotide Sequence Database Collaboration. They are classified into four genotypes which vary by geographic distribution and host range (10). In contrast, only a single serotype has been identified, suggesting that the immunodominant domain of HEV is highly conserved among genotypes. Antibodies from any one of the four genotypes cross-react with the capsid protein of genotype 1 (7).

Like other hepatitis viruses, HEV does not propagate well in currently available cell culture systems. Hepatitis E preventive strategies so far rely on the use of ORF2-derived recombinant protein (16). When expressed in insect cells, recombinant truncated ORF2 protein (PORF2), with 52 residues deleted from

---

* Corresponding author. Mailing address: Molecular and Cellular Biology, University of California, 1 Shields Ave., Davis, CA 95616. Phone: (530) 752-5659. Fax: (530) 752-3085. E-mail: rhch@ucdavis.edu.
† These authors contributed equally.

the C terminus and 111 residues deleted from the N terminus, self-assembles into virus-like particles (VLPs) (15). Our previous structural analysis of recombinant HEV VLP by cryoelectron microscopy (cryo-EM) provided the first understanding of the quaternary arrangement of PORF2.

The essential assembly element of the PORF2 protein contained amino acids 125 to 600 (13), and the reconstructed VLP displayed a T=1 icosahedral particle composed of 60 copies of truncated PORF2 (30). Recently, crystal structures were reported for genotype 1 T=1 VLPs (31), genotype 3 T=1 VLPs (32), and genotype 4 T=1 VLPs (8), revealing that PORF2 is composed of three domains, the S domain, M domain, and P domain. The T=1 icosahedral shell is composed of 60 copies of S domains, while the M domain binds tightly to the S domain and interacts with two 3-fold-related M domains to form a surface plateau at each of the 3-fold axes. Two P domains are tightly associated as a dimeric spike that protrudes from each of the icosahedral 2-fold axes. As a result, on a low-resolution cryo-EM density map, the HEV T=1 VLP appears as an icosahedral particle with 30 spikes (30).

Although these VLPs are smaller (270 Å in diameter) than the native HEV virion (320 to 340 Å), oral administration of HEV VLPs to experimental animals can induce anti-HEV antibodies that bind to native HEV (14). When a B-cell tag of 11 amino acids on glycoprotein D of herpes simplex virus was covalently coupled to the C-terminal end of PORF2 (after residue 608), the fusion protein retained the ability of PORF2 to assemble and form chimeric T=1 icosahedral VLPs that were capable of eliciting systemic and mucosal antibodies against both HEV capsid protein and the attached B-cell tag (20). Therefore, the HEV T=1 VLP is a potential carrier for delivering not only HEV antigen but also foreign antigens or antiviral drugs to the host immune system. However, rational design of HEV-based delivery vectors requires detailed information on HEV VLP structure, as well as on HEV immunodominant domains.

Here, we identified antigenic structures using cryo-EM and three-dimensional reconstruction. Our results indicate that the binding footprint of a neutralizing antibody covers the lateral side of the P domain, while a B-cell tag at the C terminus does not alter the assembly of T=1 HEV VLP.

MATERIALS AND METHODS

Production and purification of anti-HEV monoclonal antibody (MAb) MAb224. Eight-week-old female BALB/c mice were immunized at 0 and 4 weeks by intraperitoneal inoculation with HEV VLPs (100 μg/ml). Four weeks later, a final boost containing an equal volume of antigen was administered. Three days after the final boost, mouse spleen cells were fused with P3U1 mouse myeloma cells using polyethylene glycol 1500 (50% [wt/vol]) (Boehringer, Mannheim, Germany) essentially as described by Adler and Faine (1). Supernatants from microplate wells positive for hybridoma growth were screened by enzyme-linked immunosorbent assay (ELISA) using recombinant HEV VLPs as the antigen. Hybridomas that secrete antibodies specific for HEV were subcloned three times by limiting dilution, after which they were considered to be monoclonal. Antibodies in the supernatants were isotyped using a mouse monoclonal antibody isotyping kit (Amersham, Little Chalfont, Buckinghamshire, United Kingdom) in accordance with the manufacturer's protocol. Hybridomas were grown in bulk in stationary flasks (Nunc, Roskilde, Denmark) using RPMI 1640 with 15% fetal calf serum. Antibodies were purified from cell supernatants using HiTrap protein G affinity columns (Pharmacia Biotech AB, Uppsala, Sweden) and stored at −80°C. Among all of the antibodies that were generated, MAb224, an immunoglobulin G1 (IgG1) isotype, was chosen for structural analysis.

Preparation of Fab224 fragments. Isolated Fab224 fragments were prepared from purified mouse monoclonal antibodies by papain cleavage. A reducing L-cysteine buffer was used to activate the papain, and MAb224 was mixed with papain at a molar ratio of 100:1. The mixture was incubated overnight at 30°C. The reaction was stopped by the addition of iodoacetamide, and the product was analyzed by SDS-PAGE. The Fab224 fragments were purified using a 5-ml prepacked protein A chromatography column (Pierce Protein Research) according to the manufacturer's instructions. The Fc fragments and uncleaved MAb224 antibodies were trapped in the column due to their affinity for protein A, while the Fab224 fragments were collected in the flowthrough fraction.

Production and purification of anti-HEV Fab4. Fab4 was prepared by phage display and purified according to the protocol described previously (25). Briefly, chimpanzee 1441 was infected with HEV strain SAR-55. Bone marrow was aspirated from the iliac crest of this animal, and the antibody κ-chain gene and γ1-chain gene were amplified and cloned into the pComb3H phage display vector and pGEM-T cloning vector (Promega), respectively, and transformed into *Escherichia coli* XL-1 Blue. The bacteria were then amplified and infected with helper phage VCS M13 at a multiplicity of infection of 50 to produce a library displayed on the surfaces of phage particles. Phage was panned on SAR-55 ORF2-coated ELISA wells; four rounds of panning were performed. After amplification of the selected library, the phagemid DNA was extracted and the vector was modified to remove the bacteriophage coat protein III-encoding region of the phage. The phagemid DNAs were religated and transformed into *E. coli* XL-1 Blue to produce soluble Fabs. The vector pComb3H was constructed to encode a six-histidine tail at the end of the Fab fragment, thus facilitating Fab purification. Fab4 purity was determined by SDS-PAGE, followed by colloidal Coomassie brilliant blue staining.

Production and purification of HEV VLPs. The production and purification of HEV VLPs were conducted as described previously (13, 15, 20, 30). Briefly, DNA fragments encoding the N-truncated ORF2 protein (for the wild-type VLP) and the chimeric ORF2 protein (for VLP-C-tag) were cloned using the baculovirus transfer vector pVL1393 to yield pVLORF2. Insect Sf9 cells (Riken Cell Bank, Tsukuba, Japan) were used to produce recombinant baculovirus. Tn5 insect cells were infected with the recombinant baculoviruses at a multiplicity of infection of 5 and incubated in Ex-Cell 405 medium (JRH Biosciences, Lenexa, KS) for 6 days at 26.5°C. The supernatant was collected after the removal of cell debris by centrifugation at 10,000 × g for 90 min. The HEV VLPs were pelleted at 100,000 × g for 2 h in a Beckman SW32 Ti rotor and resuspended in 4.5 ml Ex-Cell 405. The VLPs were further purified by centrifugation through a CsCl density gradient (1.31 g/ml) at 110,000 × g for 24 h at 4°C in a Beckman SW 55 Ti rotor. The white virus band was collected and diluted 4 times with Ex-Cell 405 to decrease the CsCl concentration, and then the VLPs were centrifuged for 2 h in a Beckman TLA 55 rotor at 100,000 × g. The VLPs were resuspended in 100 to 500 μl of 10 mM potassium-MES (morpholineethanesulfonic acid) buffer (pH = 6.2) and stored at 4°C. To construct chimeric VLP-C-tag, recombinant baculoviruses were prepared by inserting the B-cell tag epitope from herpes simplex virus glycoprotein D (QPELAPEDPED) at amino acid position 608 (20).

Western blotting. A series of DNA fragments were constructed to encode truncated ORF2 residues 112 to 660, 112 to 608, 112 to 602, 112 to 601, 112 to 600, 112 to 596, and 112 to 589. These recombinant ORF2 genes were inserted into a baculovirus vector and expressed in insect cells using the protocol for VLP production, except that the recombinant proteins were recovered from the cytoplasm after lysis of the cell. Recombinant proteins were heated in 4× Laemmli sample buffer and electrophoresed under reducing conditions in a 10% SDS–polyacrylamide gel. After transfer of proteins to a polyvinylidene difluoride (PVDF) membrane, the membrane was blocked with TBS buffer (20 mM Tris, pH 7.6, NaCl) containing 0.5% Tween 20 (vol/vol) prior to overnight incubation with Fab224 fragments at a 1:10 dilution. After extensive washing with TBS buffer containing 0.05% Tween 20 (vol/vol), alkaline phosphatase-conjugated anti-mouse IgG (Fab specific) was incubated with the membrane for 1 h at room temperature. The blot was then washed and developed with the *p*-nitroblue tetrazolium-5-bromo-4-chloro-3-indolylphosphate (NBT-BCIP) reaction.

Preparation of VLP-Fab complexes for cryoelectron microscopy. The VLP-Fab complexes were prepared by incubating Fabs with VLPs at a molar ratio exceeding 1:300 (VLP versus Fabs) at 4°C overnight. To reduce the background density in the subsequent structural determination, highly pure VLP-Fab complexes were obtained using a short column containing Sephacryl 300, which resulted in the removal of the unbound Fab from the sample. The fractions containing VLP-Fab complexes were collected based on their optical density readings at a wavelength of 280 nm. The Fab binding occupancy was roughly estimated by performing SDS-PAGE (8-to-25% gradient) on the purified VLP-Fab complexes at a constant voltage using the Phast system (Pharmacia). The

particle morphology of VLP-Fab complexes was examined by negative-stain electron microscopy using 2% uranyl acetate.

Cryoelectron microscopy. Sample preparation and cryo-EM were performed following previously described, well-established procedures (13, 30). Briefly, a drop containing 3.5 μl of the sample was applied to a glow-discharged holey carbon-coated copper grid, blotted with a piece of filter paper for 3 s to remove the extra liquid, and quickly plunged into liquid ethane cooled by liquid nitrogen. Samples were frozen in a thin layer of vitrified ice. The grid was then transferred into a Gatan 626DH cryo holder and kept at a low temperature ($-178°C$) during the subsequent data collection. Micrographs were collected under low-dose conditions ($<10 e^-/Å^2$) using Kodak SO163 film at a magnification of $×45,000$ on an FEI CM-120 electron microscope operated at 120 kV, and particles were photographed at a defocus range of 1,000 to 3,000 nm. Micrographs were visually inspected and selected based on a suitable particle concentration, optimal ice thickness, and minimal specimen drift. Only micrographs fulfilling these criteria were analyzed.

Image processing. Selected micrographs were digitized using a Heidelberg Primescan D8200 (Heidelberg, Germany) at a 14-μm scanning step size, corresponding to 3.11 Å per pixel of specimen space. Particles were manually picked and centered by cross-correlating each one against the circular average image. The astigmatism and defocus value were evaluated by the superimposed power spectra from all particles within a single micrograph. The contrast transfer function's first zero was approximately within the range of 17 to 20 Å^{-1} for the data used for the structural determination. The self-common-lines algorithm (4) was used to yield the initial models for VLP-C-tag, VLP-Fab4, and VLP-Fab224. The origin and orientation search for each particle was carried out iteratively using the polar Fourier transformation (PFT) algorithm running on an AMD MP1800 MHz dual-processor Linux workstation (2). Three-dimensional reconstructions were computed by combining a set of particles with orientations that spread evenly in an icosahedral asymmetric unit using the Fourier-Bessel algorithm and by superimposing 5-3-2 icosahedral symmetry. To examine the reliability of the three-dimensional reconstruction, the data set was evenly divided into two parts at the final refinement step and two three-dimensional reconstructions were computed. The resolution was estimated using Fourier shell correlation (FSC) by assessing the agreement between these two reconstructions in Fourier space. Using a coefficient value of 0.5 as the criteria, the estimated resolutions of the three-dimensional reconstructions of VLP-C-tag, VLP-Fab224, and VLP-Fab4 were computed as 17.5 Å, 18.5 Å, and 24 Å, respectively.

The three-dimensional reconstructions were rendered and visualized using the Chimera program (22). The contour level was chosen at a value corresponding to 100% of the mass of the PORF2 protein. The electron density map was displayed in the isosurface mode, which builds a barrier to contour the density about a certain threshold.

Fitting the crystal structure into cryo-EM density maps. The density of the bound Fab molecule was determined from a difference density map, which was calculated by subtracting the cryo-EM map of unbound HEV T=1 VLP from the density map of the Fab-VLP complex. The cryo-EM map of unbound HEV VLP was published previously (30). Because the cryo-EM data for unbound VLP and the Fab-VLP complex were collected with the same FEI CM-120 electron microscope under similar imaging conditions, the difference density map was calculated by direct subtraction of the density of unbound VLP from the reconstruction of the Fab-VLP complex after normalizing the contrast between the two maps. The calculated difference map was used as a constraint in model fitting. Manual fitting was carried out by translational and rotational movement of the three-dimensional crystal structure of the PORF2 protein (PDB ID 2ZZQ) (31) into the cryo-EM density maps using program O (9). To obtain the best fit, the atomic model of the PORF2 subunit was treated as a rigid body. The fitting was first manually refined by minimizing the crashes between symmetry-related PORF2 molecules and then evaluated based on the cross correlation coefficient (CC value) between the cryo-EM density and the density computed from the fitted PORF2 coordinates. Fitting was halted when the CC value reached 80%. The figures were prepared using the program PyMOL (5), and the surface stereographic projection of the HEV VLP was prepared using the program RIVEM (29).

RESULTS

Binding of antibody MAb224 to PORF2. The binding of the monoclonal antibody Fab224 to PORF2 was examined via immunoblot analysis. A series of recombinant ORF2 proteins with C-terminal truncations were separated by SDS-PAGE on
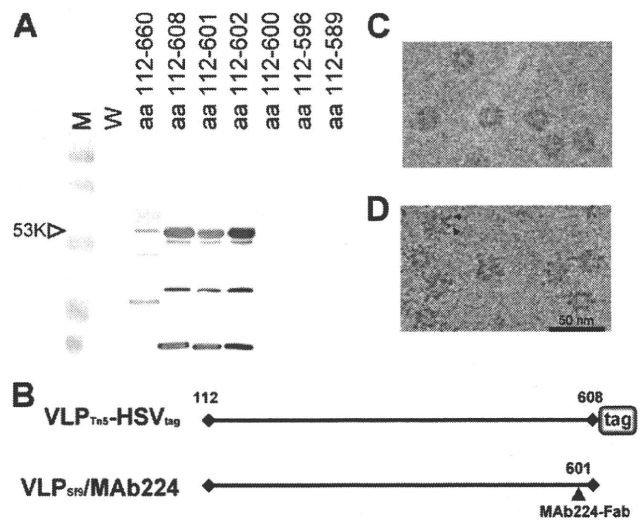

FIG. 1. Characterization of VLP-C-tag and VLP-Fab224. (A) Western blot assay of the C-terminally truncated ORF2 proteins with Fab224. M, molecular weight markers; W, peptides recovered from baculovirus-infected cells. (B) Diagram of the C-terminal markers. (C) Electron micrograph of frozen-hydrated VLP-C-tag. (D) Electron micrograph of frozen-hydrated VLP-Fab224. Black arrowheads indicate the Fab molecules attached to the VLP. Both particles showed an absence of density in the center. Note that the surface spikes in VLP-Fab224 appeared as longer thorn-like densities compared to those of VLP-C-tag.

a 10% gel under reducing conditions and blotted with Fab224 (Fig. 1A). Fab224 recognized both reduced and denatured recombinant ORF2 proteins that contained amino acids 112 to 660, 112 to 608, 112 to 602, and 112 to 601. In contrast, recombinant ORF2 proteins composed of residues 112 to 600, 112 to 596, and 112 to 589 did not bind to Fab224. These data indicate that residues 597 to 601 are critical for Fab224 binding to PORF2. Because the recombinant ORF2 proteins were recovered from cell cytoplasm where multiple forms of PORF2 were reported (15), the positive bands observed at a low molecular weight may be the proteolytic products or degraded forms of ORF2 that contain the Fab224 binding sequence.

Two-dimensional electron cryomicrographs. The chimeric VLPs (Fig. 1C) and the Fab224-conjugated VLP complex (Fig. 1D) showed circular profiles with spike-like densities that extended from the surface. As we observed previously (15, 30), they appeared to have a white, contrasting center, indicating that they are empty particles lacking RNA (data not shown). The sizes of both VLPs were approximately 27 nm without taking into account the extra densities that extended from the VLP-Fab224 surface (Fig. 1D).

Binding site of antibodies. The cryo-EM structure of HEV-Fab224 was reconstructed from 615 images of individual particles and displayed T=1 icosahedral symmetry with 60 protein subunits that were arranged into 30 dimeric protruding spikes located at each icosahedral 2-fold axis (Fig. 2A). Sixty Fab molecules were observed around each VLP particle, bound to the shoulder of the P domain. The Fab density extended ~57 Å radially away from the spike surface. The density corresponding to the Fab was approximately equal in magnitude to that of the HEV VLP, indicating that most or all of the 60
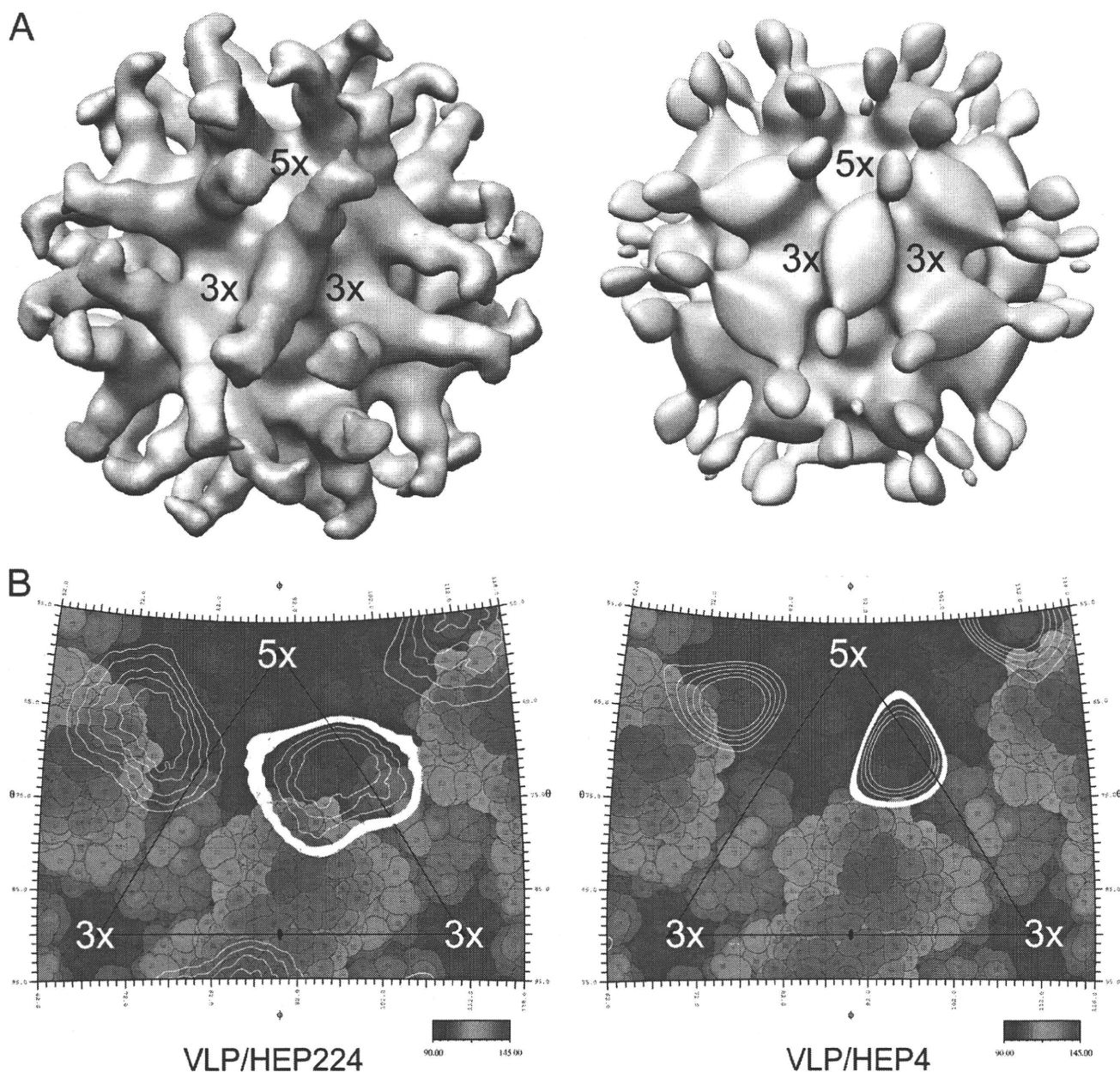
FIG. 2. The cryo-EM structure of HEV T=1 VLP in complex with anti-HEV antibodies. (A) Surface presentation of VLP-Fab224 (left) and VLP-Fab4 (right) viewed along one of the icosahedral 2-fold axes. One 5-fold axis and two adjacent 3-fold axes are marked with the corresponding number. In both reconstructions, 60 copies of Fab are attached to the lateral side of HEV VLP; however, the density of Fab4 molecules appears to be less than that of Fab224 molecules. (B) The viral surface is shown as a stereographic projection overlapped with a line drawing of an icosahedral asymmetric unit. The 5-fold and two adjacent 3-fold axes are marked with corresponding numbers, while the black triangle encloses the area of an icosahedral asymmetric unit. The surface residues are colored according to the distance from the center of the VLP, with red being the furthest away and blue representing the surface depressions. The Fab density is projected as white contour lines on the viral surface, and the outermost layer of density is drawn as thick white contour lines.

binding sites were occupied by a Fab molecule. The density corresponding to the VLP capsid was removed from the cryo-EM map, producing a Fab differential density map that was used to pinpoint the binding site of the Fab224 antibody (Fig. 3A and B).

In addition, the structure of HEV VLP in complex with the neutralizing antibody Fab4 was determined by combining 264 individual images. Fab4 precipitates both the native HEV

virion and recombinant PORF2 peptides, but the reaction depends on the presence of amino acids 597 to 607 (26). Three-dimensional reconstruction of the VLP-Fab4 complex showed 60 Fab molecules bound to each HEV VLP. Unlike the VLP-Fab224 complex, the density corresponding to Fab4 was about one-third of that of the capsid (Fig. 2A), suggesting that only 30 to 40% of the binding sites were occupied by the Fab. Moreover, the binding of Fab4 appeared to be deeper on the
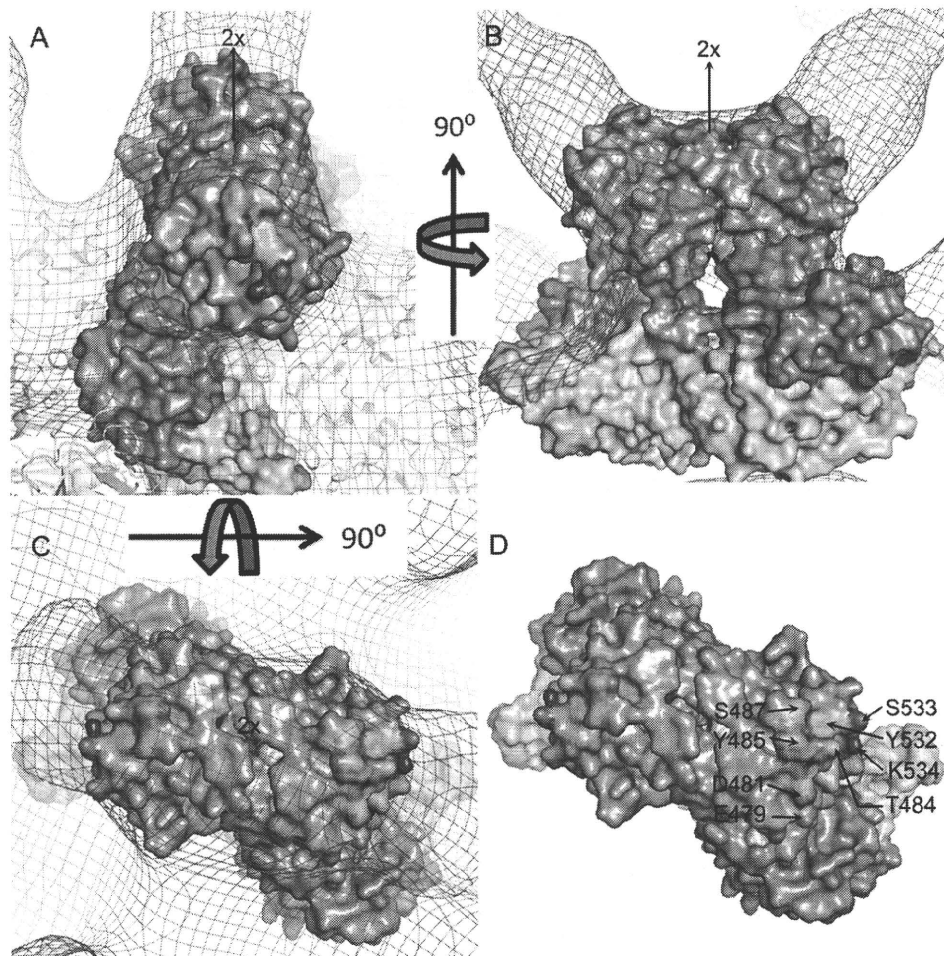
FIG. 3. The binding site of Fab224 antibody. (A) The cryo-EM density map of VLP-Fab224 was fitted with the crystal structure of PORF2 and viewed along a bound Fab molecule. One PORF2 dimer is presented as a solid surface and colored light magenta for the S domain, blue violet for the M domain, and dark gray for the P domain. The neighboring dimers are drawn in ribbon mode and colored wheat. (B) Side view of a PORF2 dimer fitted into the cryo-EM density map. (C) A PORF2 dimer viewed along the 2-fold axis and overlapped with the cryo-EM density map. (D) Top view of a PORF2 dimer viewed along the 2-fold axis. The amino acids in PORF2 responsible for binding to Fab224 are labeled. The PORF2 dimer is presented as a solid surface and colored in gray, violet, and light magenta for the P domain, the M domain, and the S domain, respectively. The residues along the Fab binding interface are colored according to the element, with green for carbon, blue for nitrogen, and red for oxygen.

side wall of the protruding domain toward the capsid shell, leaving its Fc domain exposed above the surface of the plateau (Fig. 2A). In contrast, the entire Fab224 molecule stood mainly on the top of the P domain surface. The Fab224 and the Fab4 molecules extend along the long axis of the P domain. In both cases, no steric hindrance of the Fab on the P domain with the neighboring Fab molecules at either the 5-fold or the 3-fold axes was apparent. The orientation of the Fabs relative to the plateau appeared different at a radius of 135 Å. The long axis of Fab224 tilted toward the neighboring spike, while the long axis of Fab4 pointed to the 5-fold axis (Fig. 2A).

To further analyze the Fab and HEV VLP binding interface, the crystal structure of genotype 1 PORF2 was docked onto the VLP-Fab224 cryo-EM density map. The genotype 1 PORF2 crystal structure (PDB ID 2ZZQ) is composed of three domains (31), and these domains are in good agreement with those of genotype 3 and genotype 4 PORF2 (PDB ID 2ZTN and 3HAG, respectively) (8, 32). The coordinates fitted very

well with the cryo-EM density map without any adjustment (CC value of 80%). The atoms on the surface of the HEV VLP capsid were plotted and colored according to their radial distance and overlapped with the density of the Fab at the surface plateau of the protruding spike (Fig. 2B).

The Fab224 interacted with the residues on the side of the ORF2 spike rather than with those residues on the spike's plateau surface (Fig. 3C). The contact footprint did not overlap with the dimeric interface of the PORF2 spike. As expected, Fab224 recognizes a conformational epitope, and its binding site covers a surface composed of three loops, including amino acids 470 to 493 in AB loop, amino acids 539 to 569 in CD loop, and amino acids 581 to 595 in EF loop (Fig. 3D). Residues E479, D481, T484, Y485, and S487 from the AB loop and residues Y532, S533, and K534 from the CD loop were in close contact with the Fab molecule.

Structure of HEV chimeric VLP. Chimeric HEV VLP-C-tag was constructed using a PORF2 fusion protein in which a
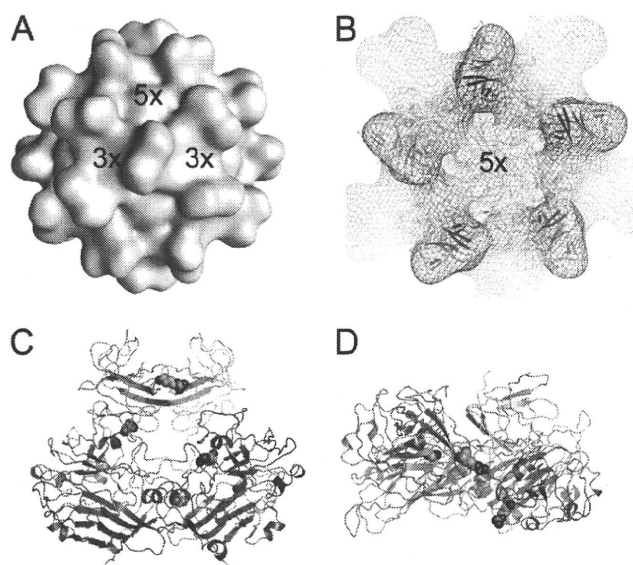
FIG. 4. The structure of the chimeric HEV VLP carrying a B-cell tag. (A) Surface presentation of VLP-C-tag viewed along an icosahedral 2-fold axis. (B) The cryo-EM density map of VLP-C-tag (mesh) was fitted with the crystal structure of the PORF2 decamer (ribbon). (C) Ribbon representation of PORF2 dimer with one monomer colored gray and the other colored pink for the S1 domain, blue for the M domain, and lime for the P domain. The amino acids prior to the four internal insertion sites are marked in sphere mode with color coding representing the elements as described in the Fig. 3 legend. (D) The top view of the PORF2 dimer, showing the location of the non-VLP insertion sites.

B-cell tag of 11 amino acids was incorporated into the C terminus of PORF2 (Fig. 1B). A total of 782 images of individual particles were used to reconstruct the final three-dimensional model of VLP-C-tag. In agreement with the previously published cryo-EM VLP structures, the surface of VLP-C-tag can

be divided into two distinct layers, an icosahedral shell and a protruding spike (Fig. 4A). The spike projects outward from the icosahedral shell and is composed of a PORF2 dimer. The distance between two adjacent spikes was ~76 Å as measured between the centers of the surface plateaus. These results are consistent with the measurements of VLPs obtained either from Tn5 insect cells (30) or from Sf9 insect cells (13), and no detectable density was added onto the outer surface of the spike. No RNA density was detected within the chimeric VLP-C-tag.

The crystal structure fit very well within the VLP-C-tag density map (Fig. 4B), indicating that the insertion of the C-terminal 11 amino acids inhibits neither the dimer-dimer interactions nor the formation of T=1 VLP. When the density maps were contoured to cover 100%, the radii of the S domains were roughly the same for both the VLP-C-tag and the VLP-Fab224 map, and the heights of the protruding spikes appeared similar. No density difference was observed from the docking (Fig. 5), suggesting that the inserted B-cell tag is flexible and less ordered. However, model fitting revealed that coordinates with unoccupied density appeared at the lateral side of the spike and underneath the Fab224 binding site (Fig. 5A and B), which may correspond to the inserted peptide.

DISCUSSION

HEV T=1 VLP is a vaccine candidate that induces protective immunity in nonhuman primates (12). It can also be used as an antigen carrier to deliver foreign epitopes through oral administration (20). Therefore, structural analysis of the antibody recognition sites is essential to suppress the neutralization effect of host vector-specific antibodies. For this purpose, we determined the structure of HEV VLP in complex with antibodies Fab224 (VLP-Fab224) and Fab4 (VLP-Fab4) and the structure of chimeric HEV VLP carrying a B-cell tag at the C terminus of PORF2 (VLP-C-tag). Docking the PORF2 crys-
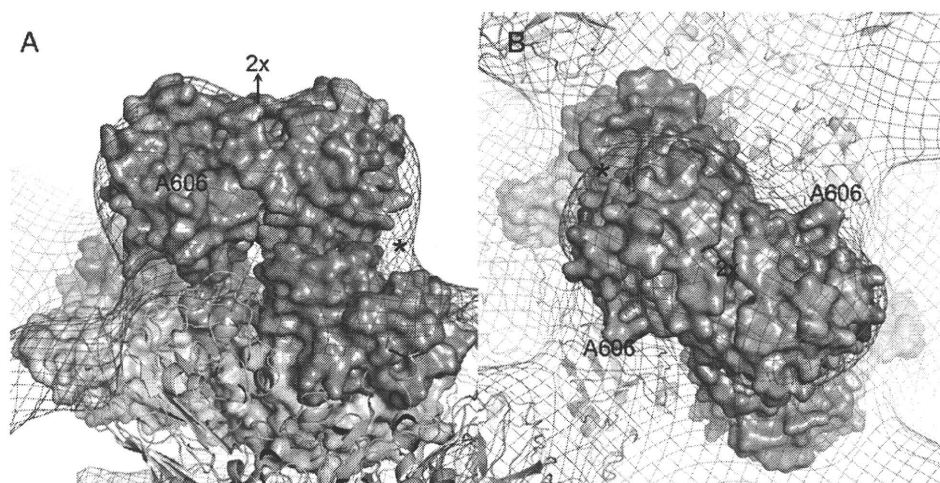

FIG. 5. Fitting of the PORF2 structure into the cryo-EM density map of HEV VLP-C-tag. The side view (A) and the top view (B) of the fitted PORF2 dimer (surface presentation) are overlapped with the cryo-EM density map of VLP-C-tag (mesh). The C-terminal residue A606 is located at the side of the protruding spike. One PORF2 dimer in the surface presentation is colored light magenta, blue violet, and gray for the S, M, and P domain, respectively. The ribbon representation shows the adjacent dimers. The amino acids in PORF2 responsible for binding to Fab224 are colored green for carbon, blue for nitrogen, and red for oxygen. Asterisks mark the location of the extra density that was not occupied with PORF2 coordinates.

tal structure provides spatial information on the HEV antigenic domain and structural guidance to better design foreign epitope insertion.

Structure of the neutralization epitopes. The antigenic properties of HEV and the mechanisms by which it is neutralized are difficult to characterize due to the lack of adequate cell culture replication systems. Therefore, our understanding of HEV immunology is mainly based on studies using recombinant proteins expressed in *E. coli* (23) and recombinant proteins or HEV VLPs generated using the baculovirus expression systems (15, 24). Data from these studies indicate that the C-terminal region of PORF2 participates in the immune response against HEV and that the HEV neutralization epitope is conformational. The minimum peptide required to induce HEV-neutralizing antibodies corresponds to a region of 148 residues in PORF2, from amino acids 459 to 607 (33). This peptide coincides with the P domain revealed in the crystal structures of PORF2. The density of the Fab in our cryo-EM structure interfaced entirely with the spikes, thus confirming that the P domain is primarily responsible for HEV antigenicity. Fab4 is a chimpanzee antibody that recognizes the ORF2 protein and was isolated from a cDNA library by using phage display (25). Fab4 binds to native HEV virions and recombinant PORF2 peptides containing amino acids 597 to 607 (26). We performed fitting with the VLP-Fab4 structure; however, the Fab4 density was too weak to conclusively determine the Fab4 binding site on the surface of HEV VLP. However, the density corresponding to the Fab4 molecule did cover amino acid 606 (data not shown). It is not clear why Fab224 appeared not to interact with peptides lacking amino acids 599 to 608 in immunoblot analysis. However, the Fab224 binding site is consistent with the critical antigenic residues determined previously using mutagenesis. It was found that double mutations that changed residues E479 and K534 or Y485 and I529 to alanine selectively abrogated PORF2's reactivity with neutralizing antibodies (11). Experiments with another set of mutants defined the same region as the HEV antigenic domain, with antibody recognition residues spreading over the AB, CD, and EF loops (32). The antibodies used in both experiments were neutralizing antibodies; therefore, the Fab224 binding surface is part of the dominant neutralization site, suggesting that the monoclonal antibody Fab224 is a neutralizing antibody. This neutralization site partially overlaps with the receptor binding site (32), and antibody binding may create spatial hindrance that prevents HEV VLPs from attaching to the cell surface.

Insertion sites for foreign epitopes. Because they are highly organized capsids that mimic the overall structure of virus particles, VLPs are a robust means by which to simultaneously carry small molecules, peptide antigenic epitopes, and DNA vaccines from heterogeneous sources to target disease sites. However, this rational vaccine design relies on excellent VLP structural information so that epitopes can be effectively conjugated to the VLP surface. In a previous study, rather than selecting PORF2 insertion sites on the basis of structural information, six insertion sites were selected according to restriction enzyme sites located either internally (four sites) or in the N or C terminus of PORF2. The internal sites are located after residues A179, R366, A507, and R542. Fusion proteins carrying insertions at sites A179 and R336 completely failed to produce VLPs, and insertions at A507 and R542 greatly re-

duced VLP production (20). Crystal structure data revealed that the spatial position of these sites is disadvantageous. Residue A179 is located in the S domain in the middle of an α-helix, which is necessary for the integrity of the S domain and its interaction with the 2-fold-related neighboring subunit. R366 is located in the M domain and favors electrostatic interaction with residue E386 from the 3-fold-related neighboring subunit. Although located within the P domain, the side chain of R542 is within the dimeric interface and guides the hydrophobic interaction of the two monomers. Replacement of R542 may misalign the orientation between two P domains and weaken the dimeric interaction between PORF2 proteins. Residue A507 in the P domain plays an important role in maintaining P domain orientation by fixing the angle of the long proline-rich hinge. Moreover, none of the four residues are exposed on the surface of VLPs, although some of them are located on the surface of individual PORF2 subunits (Fig. 4C and D). Therefore, the insertion of a foreign sequence at these sites does not interfere with the expression of individual proteins but, rather, hinders the assembly of HEV VLPs. The crystal structure revealed that the C terminus is exposed on the surface of VLPs, while the N terminus points toward the VLP center. Therefore, insertion at these two sites does not inhibit VLP assembly; however, the C terminus is more suitable for tethering bulky foreign antigenic sequences, as was shown in a previous report (20).

The cryo-EM structure of the chimeric HEV VLP-C-tag suggested that the B-cell tag was located at the lateral side of the spike, not far from residue A606 (C-terminal end in the crystal structure) (Fig. 5A). This density is located beneath the Fab224 binding site but nonetheless overlaps with the potential binding site of Fab4. As a result, the insertion of the 11-amino-acid B-cell sequence may leave the HEV antigenic site partially open and accessible to the host immune system. This explains why mice can develop antibodies against both HEV and the foreign epitope after oral administration of VLP-C-tag (20).

In conclusion, the cryo-EM structures of VLP-Fab224 identified the lateral surface of the P domain as the recognition site for anti-HEV neutralizing antibodies. The insertion of a B-cell epitope at the PORF2 C terminus does not interfere with T=1 VLP assembly. Thus, T=1 HEV VLPs are a novel tool for oral vaccine delivery, as they constitute nonreplicating entities that can induce mucosal immunity without adjuvant. The induction of antibodies against both HEV and the target disease is an additional advantage of this delivery system.

REFERENCES

1. **Adler, B., and S. Faine.** 1983. A pomona serogroup-specific, agglutinating antigen in Leptospira, identified by monoclonal antibodies. Pathology **15:** 247–250.

2. **Baker, T., and H. Cheng.** 1996. A model based approach for determining orientations of biological macromolecules imaged by cryo-electron microscopy. J. Struct. Biol. **116:**120–130.

3. **Bendall, R. P., V. Ellis, S. Ijaz, P. Thurairajah, and H. R. Dalton.** 2008. Serological response to hepatitis E virus genotype 3 infection: IgG quantitation, avidity, and IgM response. J. Med. Virol. **80:**95–101.

4. **Crowther, R. A.** 1971. Procedures for three-dimensional reconstruction of spherical viruses by Fourier synthesis from electron micrographs. Philos. Trans. R. Soc. Lond. B Biol. Sci. **261:**221–230.

5. **DeLano, W. L.** 2002. The PYMOL molecular graphics system. DeLano Scientific, Palo Alto, CA.

6. **Deshmukh, T. M., K. S. Lole, A. S. Tripathy, and V. A. Arankalle.** 2007. Immunogenicity of candidate hepatitis E virus DNA vaccine expressing complete and truncated ORF2 in mice. Vaccine **25:**4350–4360.

7. **Emerson, S., P. Clemente-Casares, N. Moiduddin, V. A. Arankalle, U. Torian, and R. Purcell.** 2006. Putative neutralization epitopes and broad cross-genotype neutralization of hepatitis E virus confirmed by a quantitative cell-culture assay. J. Gen. Virol. **87:**697–704.

8. **Guu, T., Z. Liu, Q. Ye, D. Mata, K. Li, C. Yin, J. Zhang, and Y. Tao.** 2009. Structure of the hepatitis E virus-like particle suggests mechanisms for virus assembly and receptor binding. Proc. Natl. Acad. Sci. U. S. A. **106:**12992–12997.

9. **Jones, T. A., J. Y. Zou, S. W. Cowan, and M. Kjeldgaard.** 1991. Improved method for building protein models in electron density maps and the location of errors in these models. Acta Crystallogr. A **47**(Pt. 2)**:**110–119.

10. **Khuroo, M. S., and M. S. Khuroo.** 2008. Hepatitis E virus. Curr. Opin. Infect. Dis. **21:**539–543.

11. **Li, S., S. Tang, J. Seetharaman, C. Y. Yang, Y. Gu, J. Zhang, H. Du, J. W. Shih, C. L. Hew, J. Sivaraman, and N. S. Xia.** 2009. Dimerization of hepatitis E virus capsid protein E2s domain is essential for virus-host interaction. PLoS Pathog. **5:**e1000537.

12. **Li, T.-C., Y. Suzaki, Y. Ami, T. N. Dhole, T. Miyamura, and N. Takeda.** 2004. Protection of cynomolgus monkeys against HEV infection by oral administration of recombinant hepatitis E virus-like particles. Vaccine **22:**370–377.

13. **Li, T.-C., N. Takeda, T. Miyamura, Y. Matsuura, J. C. Y. Wang, H. Engvall, L. Hammar, L. Xing, and R. H. Cheng.** 2005. Essential elements of the capsid protein for self-assembly into empty virus-like particles of hepatitis E virus. J. Virol. **79:**12999–13006.

14. **Li, T., N. Takeda, and T. Miyamura.** 2001. Oral administration of hepatitis E virus-like particles induces a systemic and mucosal immune response in mice. Vaccine **19:**3476–3484.

15. **Li, T. C., Y. Yamakawa, K. Suzuki, M. Tatsumi, M. A. Razak, T. Uchida, N. Takeda, and T. Miyamura.** 1997. Expression and self-assembly of empty virus-like particles of hepatitis E virus. J. Virol. **71:**7207–7213.

16. **Maloney, B. J., N. Takeda, Y. Suzaki, Y. Ami, T. C. Li, T. Miyamura, C. J. Arntzen, and H. S. Mason.** 2005. Challenges in creating a vaccine to prevent hepatitis E. Vaccine **23:**1870–1874.

17. **Minuk, G. Y., A. Sun, D. F. Sun, J. Uhanova, L. E. Nicolle, B. Larke, and A. Giulivi.** 2007. Serological evidence of hepatitis E virus infection in an indigenous North American population. Can J. Gastroenterol. **21:**439–442.

18. **Mushahwar, I. K.** 2008. Hepatitis E virus: molecular virology, clinical features, diagnosis, transmission, epidemiology, and prevention. J. Med. Virol. **80:**646–658.

19. **Naik, S. R., R. Aggarwal, P. N. Salunke, and N. N. Mehrotra.** 1992. A large waterborne viral hepatitis E epidemic in Kanpur, India. Bull. World Health Organ. **70:**597–604.

20. **Niikura, M., S. Takamura, G. Kim, S. Kawai, M. Saijo, S. Morikawa, I. Kurane, T. C. Li, N. Takeda, and Y. Yasutomi.** 2002. Chimeric recombinant hepatitis E virus-like particles as an oral vaccine vehicle presenting foreign epitopes. Virology **293:**273–280.

21. **Pavio, N., and J. M. Mansuy.** 2010. Hepatitis E in high-income countries. Curr. Opin. Infect. Dis. **23:**521–527.

22. **Pettersen, E. F., T. D. Goddard, C. C. Huang, G. S. Couch, D. M. Greenblatt, E. C. Meng, and T. E. Ferrin.** 2004. UCSF Chimera—a visualization system for exploratory research and analysis. J. Comput. Chem. **25:**1605–1612.

23. **Riddell, M. A., F. Li, and D. A. Anderson.** 2000. Identification of immunodominant and conformational epitopes in the capsid protein of hepatitis E virus by using monoclonal antibodies. J. Virol. **74:**8011–8017.

24. **Robinson, R. A., W. H. Burgess, S. U. Emerson, R. S. Leibowitz, S. A. Sosnovtseva, S. Tsarev, and R. H. Purcell.** 1998. Structural characterization of recombinant hepatitis E virus ORF2 proteins in baculovirus-infected insect cells. Protein Expr. Purif. **12:**75–84.

25. **Schofield, D. J., J. Glamann, S. U. Emerson, and R. H. Purcell.** 2000. Identification by phage display and characterization of two neutralizing chimpanzee monoclonal antibodies to the hepatitis E virus capsid protein. J. Virol. **74:**5548–5555.

26. **Schofield, D. J., R. H. Purcell, H. T. Nguyen, and S. U. Emerson.** 2003. Monoclonal antibodies that neutralize HEV recognize an antigenic site at the carboxyterminus of an ORF2 protein vaccine. Vaccine **22:**257–267.

27. **Tsarev, S. A., T. S. Tsareva, S. U. Emerson, S. Govindarajan, M. Shapiro, J. L. Gerin, and R. H. Purcell.** 1997. Recombinant vaccine against hepatitis E: dose response and protection against heterologous challenge. Vaccine **15:**1834–1838.

28. **Worm, H. C., and G. Wirnsberger.** 2004. Hepatitis E vaccines: progress and prospects. Drugs **64:**1517–1531.

29. **Xiao, C., and M. G. Rossmann.** 2007. Interpretation of electron density with stereographic roadmap projections. J. Struct. Biol. **158:**181–186.

30. **Xing, L., K. Kato, T. Li, N. Takeda, T. Miyamura, L. Hammar, and R. H. Cheng.** 1999. Recombinant hepatitis E capsid protein self-assembles into a dual-domain T=1 particle presenting native virus epitopes. Virology **265:**35–45.

31. **Xing, L., T. C. Li, N. Miyazaki, M. N. Simon, J. S. Wall, M. Moore, C. Y. Wang, N. Takeda, T. Wakita, T. Miyamura, and R. H. Cheng.** 2010. Structure of hepatitis E virion-sized particle reveals an RNA-dependent viral assembly pathway. J. Biol. Chem. **285:**33175–33183.

32. **Yamashita, T., Y. Mori, N. Miyazaki, H. Cheng, M. Yoshimura, H. Unno, R. Shima, K. Moriishi, T. Tsukihara, T. C. Li, N. Takeda, T. Miyamura, and Y. Matsuura.** 2009. Biological and immunological characteristics of hepatitis E virus-like particles based on the crystal structure. Proc. Natl. Acad. Sci. U. S. A. **106:**12986–12991.

33. **Zhou, Y. H., R. Purcell, and S. Emerson.** 2005. A truncated ORF2 protein contains the most immunogenic site on ORF2: antibody responses to non-vaccine sequences following challenge of vaccinated and nonvaccinated macaques with hepatitis E virus. Vaccine **23:**3157–3165.

Novel Function of CD81 in Controlling Hepatitis C Virus Replication[∇][†]

Yong-Yuan Zhang,[1] Bai-Hua Zhang,[1] Koji Ishii,[2] and T. Jake Liang[1]*

Liver Diseases Branch, National Institute of Diabetes and Digestive and Kidney Diseases, National Institutes of Health, Bethesda, Maryland 20892-1800,[1] and Department of Virology II, National Institute of Infectious Diseases, Tokyo 162-8640, Japan[2]

The mechanisms of hepatitis C virus (HCV) replication remain poorly understood, and the cellular factors required for HCV replication are yet to be completely defined. CD81 is known to mediate HCV entry. Our study uncovered an unexpected novel function of CD81 in the HCV life cycle that is important for HCV RNA replication. HCV replication occurred efficiently in infected cells with high levels of CD81 expression. In HCV-infected or RNA-transfected cells with low levels of CD81 expression, initial viral protein synthesis occurred normally, but efficient replication failed to proceed. The aborted replication could be restored by the transient transfection of a CD81 expression plasmid. CD81-dependent replication was demonstrated with both an HCV infectious cell culture and HCV replicon cells of genotypes 1b and 2a. We also showed that CD81 expression is positively correlated with the kinetics of HCV RNA synthesis but inversely related to the kinetics of viral protein production, suggesting that CD81 may control viral replication by directing viral RNA template function to RNA replication. Thus, CD81 may be necessary for the efficient replication of the HCV genome in addition to its role in viral entry.

Hepatitis C virus (HCV) infection affects about 170 million people worldwide. Chronic HCV infection is an important cause of liver diseases, leading to cirrhosis and hepatocellular carcinoma (2, 18). The therapy for chronic HCV infection to date is suboptimal and associated with many side effects (12, 13). The mechanisms of HCV replication and persistent infection remain poorly understood (3, 31).

HCV carries a positive- and single-stranded RNA genome consisting of approximately 9,600 nucleotides (nt) (36). HCV encodes 10 proteins and exploits cellular factors for replication (24, 32, 35, 41). However, many crucial host factors required for HCV RNA replication remain undefined. The HCV RNA genome, like other positive-stranded RNA viruses, serves as templates for both viral protein translation and RNA replication (4, 15, 28), which are expected to be asynchronous *in vivo*, as the template pool is constantly replenished from ongoing HCV infection and replication (4). However, a coordinated translation/transcription process would be predicted if the use of HCV RNA as a template is subjected to cellular factor control that directs HCV RNA for specific template functions and synchronizes the translation/transcription process. CD81 has diverse functions in various biological processes (23, 39, 48) and is known to mediate HCV entry (10, 30, 34, 49). CD81 was recently suggested to play a role in postentry events (8). In this study we identified CD81 as a key cellular factor required for efficient HCV RNA replication, and inefficient RNA replication occurs in HCV-infected or RNA-transfected cells with

low levels of CD81. Our data also showed that the utilization of HCV RNA as templates for viral protein synthesis and RNA synthesis is mutually exclusive and suggested that HCV RNA template function for RNA replication may be subjected to CD81 control.

MATERIALS AND METHODS

Plasmids. The HCV JFH1 full cDNA sequence cloned into plasmid pUC19 (pJFH-1) and the JFH1 subgenomic replicon plasmid (pSGR-JFH1/Luc) were described previously (46). Plasmid pJ6/JFH1-p7Rluc2A (20) was a gift of Charlie Rice (Rockefeller University). pHCV-FLuc-3′-UTR, containing the firefly luciferase gene driven by the HCV internal ribosome entry site (IRES), was provided by Michael Niepmann (40). The human CD81 gene-carrying plasmid (pCDM8hCD81) (33) was a gift of Shoshana Levy (Stanford University, Stanford, CA). The CD81 mutant construct was generated by PCR-based mutagenesis that converted the methionine coding codon (AGT) to a stop codon (TAG) in the reading frame. The primers used were sense primer ATC AAG TAC CTG CTC TTC GTC TAG AAT TTC GTC TTC TGG CTG and antisense primer TGT TCT TGA GCA CTG AGG TGG TCA AAG CAG. The lack of CD81 expression was verified by CD81 staining after transfection with this construct.

Cell lines and culture. Huh7.5 cells (7) maintained in our laboratory contain less than a 50% CD81-positive population. To obtain cell populations with different percentages of CD81-positive cells, three populations were selected from Huh7.5 cell by fluorescence-activated cell sorter (FACS) sorting: a CD81 high-level population (CD81-H), with 90% CD81-positive cells; CD81 low-level population 1 (CD81-L1), with 10% CD81-positive cells; and CD81 low-level population 2 (CD81-L2), with no detectable CD81 expression. All three populations were subjected to the same culture conditions as those used for the Huh7.5 cells. The cells were expanded, cryopreserved, and thawed for subsequent experiments. Continuous passages of these cells were avoided because of concern for altered phenotypes during long-term culture. Typically, these cells were not passaged more than 10 times after thawing. CD81 expression profiles for the three populations were monitored by FACS for CD81 expression after the reestablishment of cryopreserved cells and during experiments. The phenotype of CD81 expression remained stable during this short-term culturing. For FACS analysis, cells were trypsinized and then washed with magnetic cell sorting (MACS) buffer containing phosphate-buffered saline (PBS), bovine serum albumin (BSA), EDTA, and 0.09% azide (pH 7.2) (Miltenyi Biotec Inc., Auburn, CA). Approximate 10^6 cells were suspended in 100 μl MACS buffer, mixed with 10 μl fluorescein isothiocyanate (FITC)-conjugated anti-human CD81 (JS-81; BD Pharmingen) or 10 μl FITC-conjugated mouse IgG1 as an isotype control

* Corresponding author. Mailing address: Liver Diseases Branch, National Institute of Diabetes and Digestive and Kidney Diseases, National Institutes of Health, 10 Center Drive, Rm. 9B16, Bethesda, MD 20892-1800. Phone: (301) 496-1721. Fax: (301) 402-0491. E-mail: jakel@bdg10.niddk.nih.gov.

(BD Pharmingen), incubated on ice for 20 min, washed twice with MACS buffer, and suspended in 400 μl MACS buffer for FACS analysis. FACS for Sr-B1 expression was performed with mouse monoclonal anti-human CLA-1 (BD Transduction Laboratories).

The Huh7-25 clone and subgenomic HCV replicon cell lines Huh7/Rep-Feo (genotype 1b) and pSGR-JFH1-C4/1 (genotype 2a) were described previously (1, 25, 43). Another subgenomic HCV JFH1 replicon cell line, SGR-JFH1-FLuc/Neo, expressing FLuc-neo as the reporter, was generated similarly. All replicon cells were maintained in the presence of 500 μg/ml of G418 (Invitrogen).

siRNA and transfection. The CD81 small interfering RNA (siRNA) pool (siGenome SMARTpool Duplex catalog numbers D-017257-01, -03, -04, and -05) and nontarget control 2 siRNA (catalog number D-001810-02-05) were purchased from Dharmacon Inc. siRNA transfection was carried out in 12-well plates with Oligofectamine reagents (Invitrogen), and the final siRNA concentration was 50 nM.

Production of HCV pseudovirus and HCV JFH1 virus and viral inoculation. The HCV pseudovirus (H77 strain) was a gift of C. M. Rice (Rockefeller University). HCV pseudoparticle (HCVpp) infection and measurement of infectivity were described previously (14). For the transfection of JFH1 HCV RNA, cells were plated onto a 6-well plate at 1.5×10^5 cells per well overnight. Cells were washed twice with PBS after the medium was removed, and 1 ml Opti-MEM (Invitrogen) was added. Transfection mix containing 1,000 μl Opti-MEM, 12 μl DMRIE-C (1,2-dimyristyloxypropyl-3-dimethylhydroxy ethyl ammonium bromide-cholesterol) (Invitrogen), and 10 μg *in vitro*-transcribed JFH1 RNA was then added to cells and incubated for 4 h. Opti-MEM was then replaced with regular Dulbecco's modified Eagle's medium (DMEM). Media containing high titers of HCV (from day 3 to day 7) were collected as an initial inoculum. For HCV infection, Huh7.5 cells were plated onto 6-well plates at 1.5×10^5 cells per well overnight. The cells were inoculated with cell culture-derived HCV (HCVcc) as described above. The inoculum was removed at day 1 postinoculation (p.i.), and the infected cells were transferred onto a 10-cm dish at day 3 p.i. The media were collected and pooled together from days 4 to 7. The medium containing high-titer HCV was aliquoted and stored at −80°C as an inoculum. The inoculum was used at a multiplicity of infection (MOI) of 200:1 (based on the number HCV RNA genome copies per cell). In our experience, one infectious unit is equivalent to about 200 to 500 HCVcc RNA genome copies.

HCV RNA and core antigen assays. Trypsinized cells were washed with PBS once, and RNA was extracted by using Trizol (Invitrogen). RNA was resuspended in 50 μl diethyl pyrocarbonate (DEPC)-H2O, and the final concentration was adjusted at 0.1 μg RNA/μl. Three microliters of RNA was used for quantitative reverse transcription (RT)-PCR (q-RT-PCR), and HCV RNA copies were expressed as copies per μg RNA. For the extraction of RNA in the medium, 250 μl medium was mixed with 750 μl Trizol LS (Invitrogen) according to instructions provided by the manufacturer. RNA was resuspended in 50 μl DEPC-H2O. Three microliters of RNA was used for q-RT-PCR, and HCV RNA copies were normalized as copies per ml medium. HCV RNA q-RT-PCR was described previously (42). The primers and TaqMan probe used for CD81 RNA quantification were sense primer AGG GCT GCA CCA AGT GC, antisense primer TGT CTC CCA GCT CCA GAT A, and TaqMan probe sequence 5′-6-carboxyfluorescein (6-FAM)-CAA GTA CCT GCT CTT CGT CTT CAA-6-carboxytetramethylrhodamine (TAMRA)-3′. For minus-strand RNA detection we applied a method described previously by Lanford et al. (27). A sense primer (GCG TTA GTA TGA GTG TCG TAC AGC, at nt 87 to 110 of the 5′ untranslated region [UTR] of the JFH1 genome) was used to synthesize cDNA from the minus-strand RNA templates at 70°C by r*Tth* DNA polymerase (Applied Biosystems). The reverse transcription activity of r*Tth* was blocked by adding buffer chelating MnCl2, and the DNA polymerase activity was facilitated by including MgCl2-containing buffer after the RT reaction. q-RT-PCR was performed for the detection of total HCV RNA.

For intracellular core determinations, approximately 300,000 cells were suspended with 100 μl lysis buffer (pH 7.5) (20 mM Tris, 1% NP-40, 1% Na deoxycholate, 0.1% SDS, and 1× protease inhibitor cocktail) and incubated on ice for 20 min. The supernatant was transferred into a new tube after a brief spin to remove cell debris. Ten microliters of supernatant was diluted 10-fold for core protein enzyme-linked immunosorbent assay (ELISA) (Ortho). The total amount of intracellular core protein was expressed as attomoles per well. A similar amount of uninfected cells at each time point was harvested and prepared in the same way as that for the infected cells for a negative control in ELISA tests. For extracellular core determinations, 5 μl of culture supernatant was diluted 20-fold and used for core ELISA. The core protein in the medium was expressed as attomoles/ml.

Single-cell-based q-RT-PCR assay. The assay for single-cell HBVcc cDNA quantification was described previously (50, 51). Briefly, trypsinized cells were

suspended in DMEM and counted. The initial cell concentration in the suspension was approximately 10^5 cells/ml. The cell suspension was then subjected to two steps and 100-fold dilutions with buffer containing 150 mM Tris-HCl (pH 8.0), 1 mM EDTA, and 10 mM NaCl. The cell suspension concentration was then further adjusted to 100 cells per ml. Ten microliters of cell suspension containing approximately a single cell was manually distributed into each of the 96 wells of the plate. Ten microliters of proteinase K solution was added to each well (final concentration, 2 mg/ml) and incubated at 50°C for 60 min, and proteinase K was inactivated at 75°C for 15 min. Ten microliters of solution was transferred from each well onto a new plate. One plate was used for HCV RNA, and the other was used for CD81 RNA q-RT-PCR.

RESULTS

Divergent levels of HCV RNA in various CD81-expressing cells after HCV infection. To investigate HCV infection and replication efficiency in cells with different CD81 expression levels, two cell populations, CD81-high (CD81-H) and CD81-low 1 (CD81-L1), containing 90% and 10% CD81-positive cells, respectively, were first isolated from Huh7.5 cells through cell sorting. A third cell population containing barely detectable CD81 expression was isolated from CD81-L1 cells and designated CD81-L2. The difference in CD81 expression levels detected by FACS was also confirmed by CD81 RNA quantification among three cell lines (Fig. 1A and B). CD81-H and CD81-L1 cells not only differ by the percentages of CD81-positive cells but also differ in CD81 expression intensities by relative mean fluorescence intensities (rMFIs) (up to 4-fold difference) (Fig. 2B). The CD81 expression profiles of the various cell lines determined by FACS were similar to those found in a study reported previously, in which Huh7-derived clones with variable CD81 expression levels were selected (1). CD81 expression levels did not increase appreciably after the permeabilization of cells before staining, indicating that most of the expression was on the cell surface (see Fig. S1 in the supplemental material). No major difference in SR-BI expression levels was detected among the parental Huh7.5 cell line and its derived cell lines (Fig. S2). Each cell population was inoculated with the same-size inoculum (MOI of 200:1 based on the number of HCV genome copies per cell). The intracellular HCV RNA level was determined at day 6 postinoculation (p.i.) by quantitative RT-PCR (q-RT-PCR). As shown in Fig. 1C, a >200-fold difference in HCV RNA levels was found between CD81-H and CD81-L1 cells, whereas no HCV RNA was detectable in CD81-L2 cells (detection limit of 10^3 copies/ml). The difference was initially thought to result from the difference in the percentages of CD81-positive cells, assuming that only cells with detectable cell surface CD81 expression levels could be infected by HCV (1). It would take multiple rounds of infection to have all 90% of the CD81-positive cells infected in CD81-H cells. We reasoned that a 9-fold difference in CD81-positive cells might not explain the >200-fold difference in HCV RNA levels between CD81-H and CD81-L1 cells and the even bigger difference between CD81-H and CD81-L2 cells, suggesting that the infected CD81-H cells might support higher HCV replication in addition to the difference in the number of infected cells.

Additional role of CD81 in HCV RNA replication other than viral entry. There are two possible explanations (or a combination of both) for the higher HCV RNA level in infected CD81-H cells: CD81-H cells support more efficient HCV entry, or CD81-H cells support more efficient HCV RNA repli-
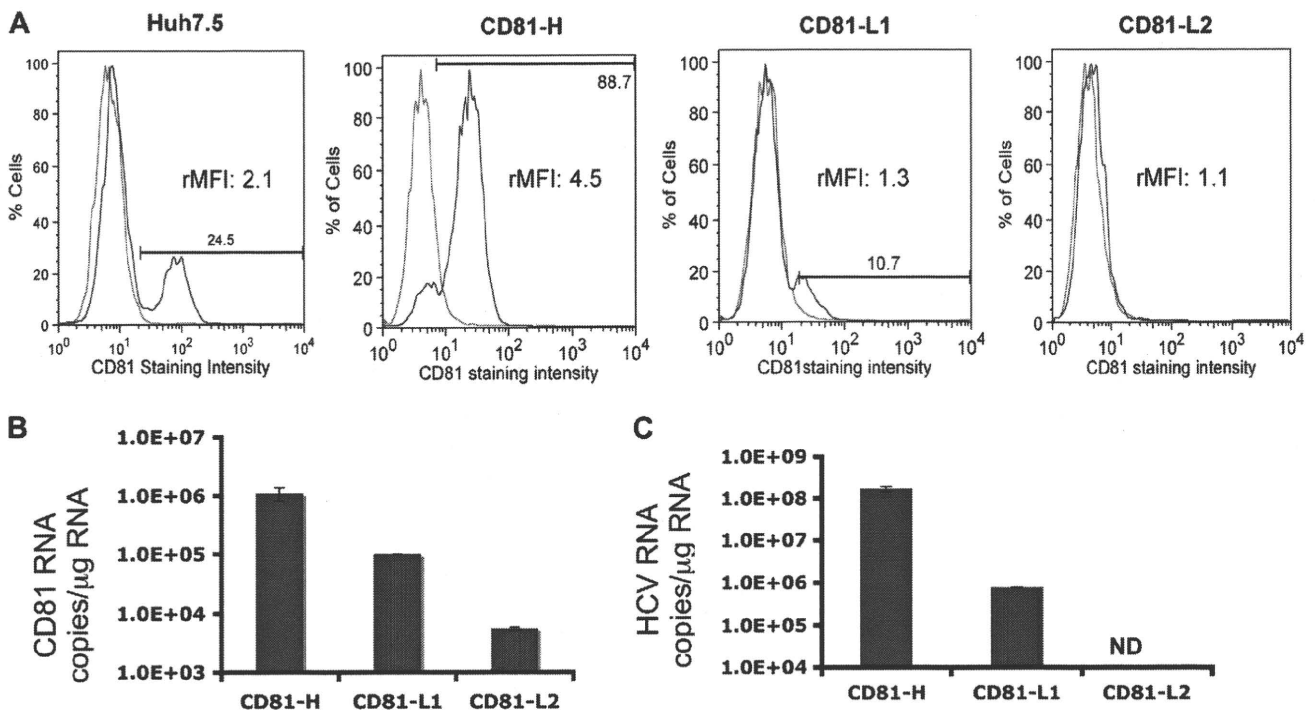
FIG. 1. CD81 expression and HCV RNA levels among the three Huh7.5 cell populations. CD81 cell surface expression and CD81 RNA levels of the three cell lines were monitored regularly, and representative profiles are shown. (A) Percentages of CD81-positive cells detected by FACS (blue, CD81; red, isotype IgG1). The relative mean fluorescence intensity (rMFI) (ratio of the CD81 mean fluorescence intensity over the IgG1 control mean fluorescence intensity in the same cell population) of each cell population is shown. (B) CD81 RNA expression level determined by q-RT-PCR. (C) Intracellular HCV RNA level in CD81-H, CD81-L1, and CD81-L2 cells detected by q-RT-PCR at day 6 p.i. with JFH1 HCVcc. ND, not detectable. Mean values (triplicates) ± standard deviations (SD) are shown. Data from one of three independent experiments are shown.

cation. To investigate these two possibilities, CD81-H, CD81-L1, and CD81-L2 cells were tested for HCV entry efficiency by the HCVpp assay (6, 14). The three cell lines did not show any significant differences in HCVpp infectivity (Fig. 2A) despite a 4-fold difference in the CD81 rMFI (Fig. 2B) among the populations tested. It is noteworthy that the CD81 expression level in CD81-positive cells fluctuates periodically. CD81 expression levels showed a 2-fold reduction in rMFI (Fig. 2B) in the retesting of CD81-H cells with HCVpp infection. No corresponding reduction of HCVpp entry efficiency was observed. HCVpp infectivity was significantly suppressed by anti-CD81 antibodies in all cells tested, indicating that CD81 is indeed important for viral entry (Fig. 2A). Although the three cell lines did not show major differences in HCVpp infectivity, the CD81-L2 cells did show somewhat lower luciferase activities in the HCVpp assay than the CD81-H cells, suggesting that the very low level of CD81 may be affecting viral entry.

To further investigate viral entry efficiency, each cell population was inoculated with HCVcc. HCV-infected cells were harvested by trypsin treatment and extensive washing to eliminate surface-bound virus (8) at 4 h p.i., and the intracellular HCV RNA level was determined. There was no difference in HCV RNA levels among the three populations (Fig. 2C).

The HCVcc entry data were confirmed by infection with HCVcc containing the luciferase reporter gene (20). The luciferase activity was measured at 24 h p.i., and no difference was detected among the three cell populations tested (Fig. 2D). Both HCVpp and HCVcc data suggest that cells with high

CD81 levels do not facilitate more HCV entry. This finding prompted us to consider that high levels of CD81 expression might not be sufficient to increase viral entry efficiency if other cellular factors (37) involved in HCV entry, like SR-BI (5), were limiting (see Fig. S2 in the supplemental material). It was shown previously that HCVcc or HCVpp can enter into cells with low levels of CD81 (1, 26, 52), and cells with different CD81 levels have no noticeable differences in initial HCV infection (26). It is conceivable that a threshold of CD81 expression is necessary for viral entry and that beyond this threshold, more efficient viral entry does not occur. This observation of a CD81 threshold level was already suggested previously (26). Thus, our data suggest that the high level of HCV RNA in CD81-H cells may result from a more efficient HCV RNA replication.

To study whether cells with higher CD81 levels support more efficient RNA replication, we investigated whether HCV RNA replication efficiency is correlated with the CD81 level at the single-cell level. Both HCV RNA and CD81 RNA levels were determined for the same cells harvested on days 3 and 6 p.i. by a single-cell-based RNA quantification technique (50, 51). Figure 3A shows the distribution patterns of CD81 RNA and HCV RNA copies per cell at day 6 p.i. The highest level of CD81 RNA per cell was 3,600 copies, while the lowest was under 100 copies. HCV replication efficiencies differed significantly among individual cells. The highest level of HCV RNA per cell was 89,600 copies. Average HCV RNA copies per cell increased by 13-fold, from 320 to 4,300 copies in cells with an
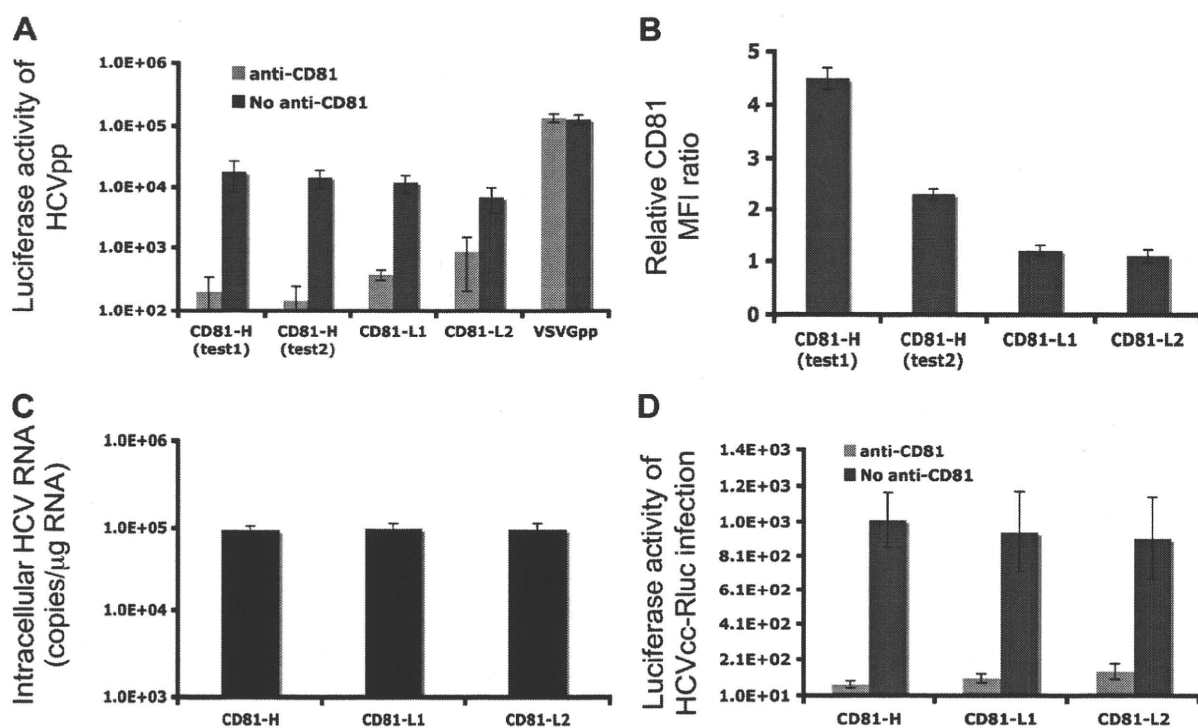
FIG. 2. Similar efficiencies of viral entry among the three Huh7.5 cell populations. (A) Luciferase activities measured at 48 h after HCVpp inoculation. Shown are mean values (triplicates) ± SD. (B) The CD81 relative mean fluorescence intensities (MFI) among the three cell populations were monitored. Significant differences in rMFI among the cell populations exist ($P = 0.0084$ for CD81-H in test 1 versus test 2 and $P = 0.0026$ and $P = 0.00056$ for CD81-H in test 1 versus CD81-L1 and versus CD81-L2, respectively). (C) Intracellular HCV RNA level determined at 4 h p.i. by q-RT-PCR. Cells were harvested by 8 min of trypsin treatment that removes almost all bound viruses but not internalized viruses (data not shown). (D) Luciferase activities measured at 24 h postinfection with HCVcc containing the luciferase gene generated from pJ6/JFH1-p7Rluc2A. Shown are mean values (triplicate) ± SD. Data from one of three independent experiments are shown.

average of 400 CD81 RNA copies between days 3 and 6 p.i. (Fig. 3B). For cells with an average of 1,800 CD81 RNA copies, the average number of HCV RNA copies increased by more than 200-fold, from 130 to 35,000 copies, over the same time period (Fig. 3C). The relationship between CD81 RNA and HCV RNA levels in the same individual cells was further analyzed. As shown in Fig. 3C, there was a positive correlation between CD81 RNA and HCV RNA levels in the same cells on day 6 p.i. ($P < 0.0001$), suggesting that HCV RNA replication efficiency is dependent on the CD81 level in individual cells. In contrast, the percentage of HCV-infected cells, as demonstrated by a single-cell assay, did not show a corresponding difference between high-level and low-level CD81-expressing cell populations (Fig. 3D). In fact, a somewhat higher percentage of lower-level CD81-expressing cells was positive for HCV RNA.

CD81-L cells do not support efficient viral replication after viral protein synthesis. To determine whether CD81-L cells support efficient HCV RNA replication, CD81-H, CD81-L1, and CD81-L2 cells were transfected with JFH1 subgenomic replicon RNA containing the luciferase gene. The cells were harvested for determinations of luciferase activities and HCV RNA levels at various time points. As shown in Fig. 4A (left), there were no differences in luciferase activities among all cells tested up to day 2 posttransfection. However, efficient HCV RNA replication was detected for CD81-H but not CD81-L cells, as reflected by the decreasing HCV RNA levels in

CD81-L and Huh7-25 cells (Fig. 4A, right). To exclude the possibility that the requirement of high levels of CD81 for HCV RNA replication is a unique feature of the Huh7.5 cell lines that we selected, a different Huh7 cell clone (Huh7-25) with little CD81 expression (1) (see Fig. S4A in the supplemental material) was tested, and a result was obtained that was similar to that for the CD81-L2 cells. Equally efficient protein translation in CD81-L1 and CD81-L2 cells was further demonstrated by the transfection of a construct containing the luciferase reporter gene under the control of the HCV IRES (40) (Fig. 4B).

We investigated the difference in the RNA replication efficiencies during the first 24-h period after cells were transfected with JFH1 subgenomic RNA or JFH1 genomic RNA. As shown in Fig. 4C and D, a 10-fold difference or more in intracellular or extracellular HCV RNA levels was detected between transfected CD81-H and CD81-L2 cells. In addition, HCV minus-strand RNA was detected only in the CD81-H cells. These data indicate that these cells support protein synthesis equally after RNA transfection, but cells with low levels of CD81 do not support efficient HCV RNA replication. It also raises the interesting possibility that HCV protein reporter constructs, like luciferase, may not necessarily reflect the HCV RNA replication status in certain situations.

Viral protein synthesis and RNA replication were also tested with infected cells. Intracellular core protein and HCV RNA levels were analyzed at different time points after infection of
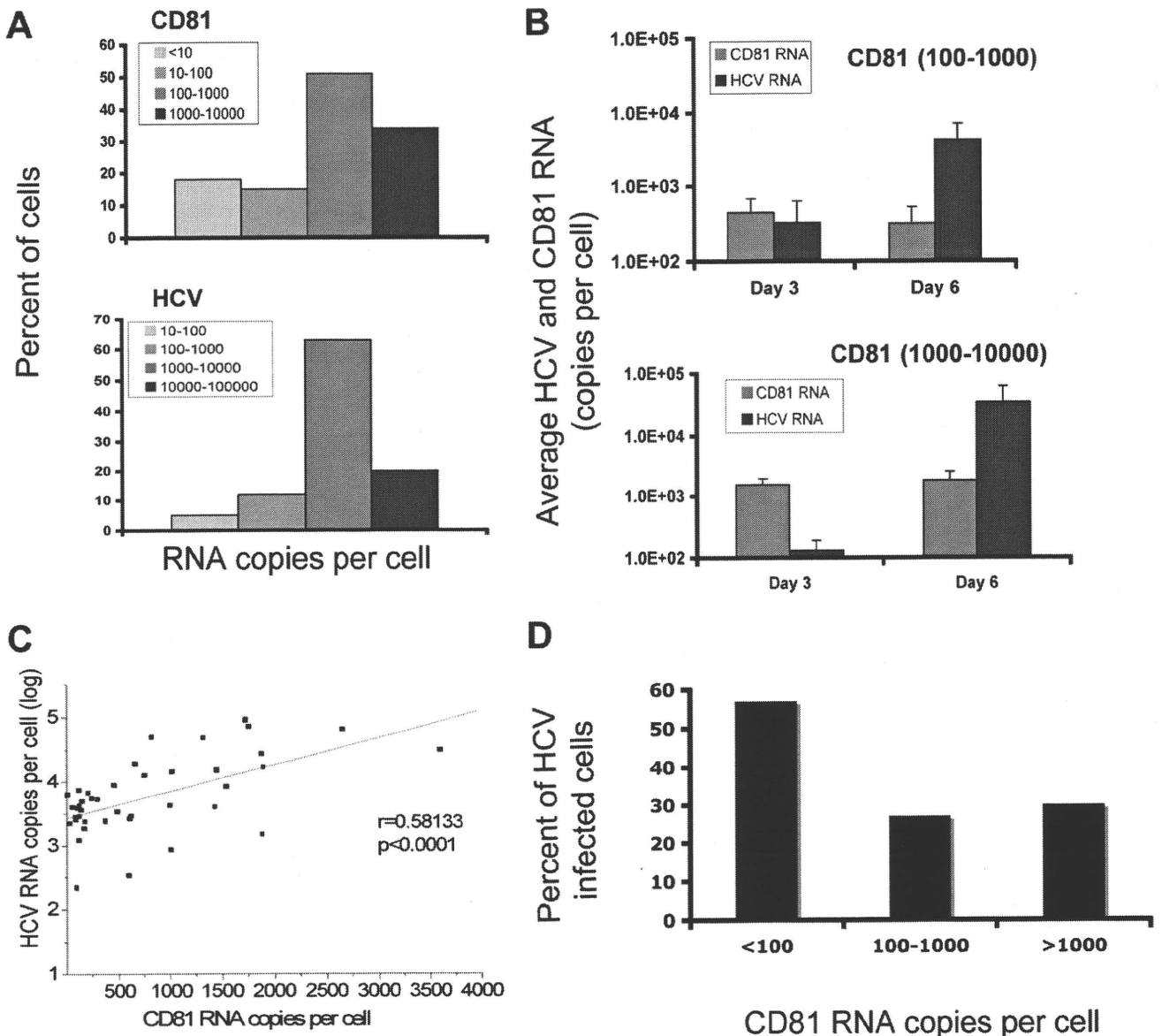
FIG. 3. Single-cell correlation of HCV RNA and CD81 levels. Huh7.5 cells were infected with HCVcc and subjected to a single-cell-based q-RT-PCR assay. (A) Distribution of CD81 and HCV RNA copies/cell measured at day 6 p.i. for individual cells. (B) HCV and CD81 RNA levels were determined on days 3 and 6. Cells were divided into those with 100 to 1,000 (top) and those with 1,000 to 10,000 (bottom) CD81 copies/cell and plotted for their corresponding numbers of HCV RNA copies/cell. (C) Correlation of HCV RNA with CD81 RNA copy numbers of individual cells on day 6 p.i. ($r = 0.58133$ and $P < 0.0001$, determined by use of Microcal Software Inc.). (D) Percentage of HCV infection in cells with different CD81 levels. Infected cells were harvested at day 3 p.i., and HCV RNA levels and CD81 RNA copy numbers in the same cells were determined. The percentage of infection in each group was calculated by dividing the number of cells with detectable HCV RNA by the number of the total cells in each of three populations that contained <100, 100 to <1,000, and >1,000 copies of CD81 RNA per cell.

CD81-H, CD81-L1, and CD81-L2 cells. Consistent with data shown in Fig. 4A, the core protein levels were similar among infected CD81-H, CD81-L1, and CD81-L2 cells on days 2 and 3 (Fig. 5A), suggesting that CD81-L cells are capable of supporting viral protein synthesis after viral entry. The newly synthesized core protein detected by ELISA was further verified by core-staining-positive cells in these cells. As many as 27% of CD81-L2 cells became core positive on day 3 (see Fig. S3 in the supplemental material) but not on day 1 (data not shown), suggesting that the detected core protein was newly synthe-

sized in infected CD81-L2 cells. However, little HCV RNA replication occurred in infected CD81-L2 cells, while only modest HCV RNA replication was detected for CD81-L1 cells (Fig. 5B). These data suggest that efficient HCV RNA replication did not occur in CD81-L cells despite active viral protein synthesis. In contrast, efficient HCV RNA replication occurred in CD81-H cells with HCV RNA levels 10-fold and 1,000-fold greater than those of CD81-L1 cells at 24 h and on day 6 p.i., respectively (Fig. 5B), suggesting that viral replication proceeds efficiently in CD81-H cells.
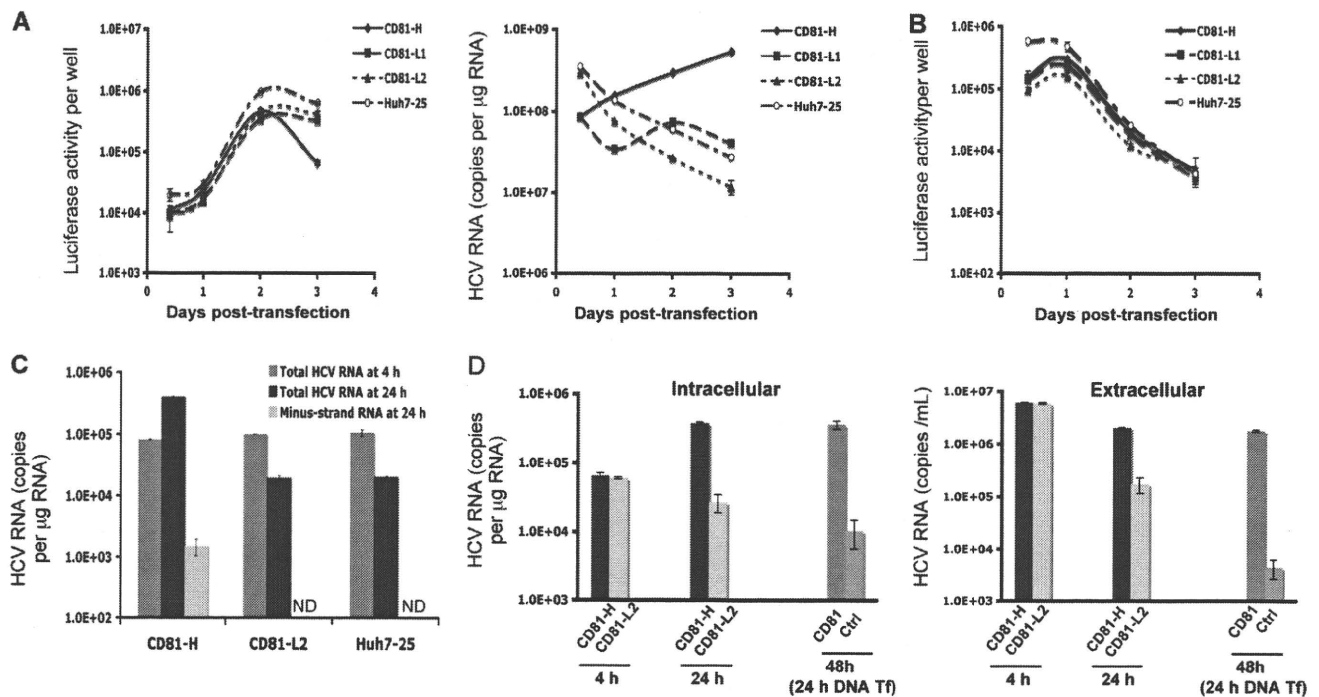
FIG. 4. Protein synthesis and RNA replication among cell populations with different CD81 levels. (A) Luciferase activities (left) and HCV RNA levels (right) measured at different time points after JFH1 subgenomic replicon RNA (pSGR-JFH1/Luc) transfection (Tf) of Huh7.5 cells. Shown are mean values (triplicates) ± SD. (B) Luciferase activities of Huh7.5 cells after transfection with a construct containing the luciferase gene driven by the HCV IRES (pHCV-FLuc-3′-UTR). Mean values (triplicates) ± SD are shown. (C) Intracellular total and minus-strand RNA levels at 24 h after pSGR-JFH1/Luc RNA transfection. Cells were transfected and harvested at 4 and 24 h. The total and minus-strand HCV RNA levels were determined by q-RT-PCR. The minus-strand HCV RNA assay has a detection limit of about 500 to 1,000 copies/µg of total RNA. ND, not detected. (D) Intracellular and extracellular RNA levels at 24 h after transfection with JFH1 genomic RNA. CD81-H and CD81-L2 cells were first transfected with JFH1 RNA, and cells and medium were harvested 4 and 24 h later for determinations of HCV RNA levels. Another set of CD81-L2 cells was transfected with a CD81 expression plasmid at 24 h after JFH1 RNA transfection and harvested 24 h later (48 h after JFH1 RNA transfection) for HCV RNA determinations as described above. Mean values ± SD are shown. Data from one of two independent experiments are shown.

The difference in HCV RNA replication levels between CD81-L1 and CD81-H cells was further demonstrated by analyzing the distribution of newly synthesized core protein. A larger amount of core protein was detected intracellularly in CD81-L1 cells from days 1 to 3 p.i., while more core protein was detected extracellularly in CD81-H cells during the same time period (Fig. 5C), suggesting that CD81-L1 cells were infected by HCV and supported viral protein synthesis. However, the synthesized core protein was mainly intracellular and accumulated to a higher level in CD81-L1 cells. In contrast, the synthesized core protein in CD81-H cells was efficiently exported to the medium, probably in the form of virions, as a result of active HCV RNA replication. This observation was further supported by the kinetics of intracellular and extracellular HCV RNA levels after infection. Both intracellular and extracellular HCV RNA levels in CD81-H cells were 100-fold higher than those in CD81-L1 cells later in the infection (Fig. 5D).

Ectopic expression of CD81 leads to efficient HCV RNA replication in CD81-L cells. To test directly whether high levels of CD81 are required for efficient HCV RNA replication, CD81-L2 cells were first transfected with the JFH1 subgenomic replicon or JFH1 genomic RNA and then transfected with a CD81 expression plasmid or vector 1 day later. As

shown in Fig. 4D and 6A, CD81-L2 cells showed decreasing HCV RNA levels after HCV RNA transfection, suggesting a lack of efficient HCV RNA replication. In contrast, following CD81 DNA transfection, CD81-L2 cells showed significantly increasing HCV RNA levels, similar to CD81-H cells, suggesting that HCV RNA replication was restored in CD81-L2 cells after CD81 transfection. To further explore the role of CD81 in viral replication, CD81-L2 cells were first infected with HCV, and after infection, cells were washed extensively and replated onto 6-well plates on day 1 p.i. The replated cells were then transfected with a CD81 expression plasmid on day 2 p.i. Cells were harvested at various time points to determine HCV RNA levels. As shown in Fig. 6B, infected CD81-L2 cells did not support HCV RNA replication at all. In contrast, CD81-L2 cells transfected with CD81 after inoculation demonstrated a rapid increase in HCV RNA levels. The kinetics of the increase suggest that this early increase likely occurs at the replication level. It is unlikely that this rapid increase is the effect of CD81 transfection on HCV entry because CD81-mediated HCV entry should occur within 1 h of infection (11, 17). However, the later increase probably represents the additional effect of enhanced CD81-dependent viral spread. These data provide direct evidence that a high level of CD81 is required for efficient HCV RNA replication and that the inability of